

# Two Fluid Space-Time Discontinuous Galerkin Finite Element Method. Part II: Applications

W.E.H. Sollie, J.J.W. van der Vegt\*

*Department of Applied Mathematics, Institute of Mechanics, Processes and Control  
Twente, University of Twente, P.O.Box 217, 7500 AE, Enschede, The Netherlands*

---

## Abstract

The numerical method for two fluid flow computations presented in Sollie, Bokhove & van der Vegt, Two Fluid Space-Time Discontinuous Galerkin Finite Element Method. Part I: Numerical Algorithm (submitted to Computer Methods in Applied Mechanics and Engineering) is applied to a number of one and two dimensional single and two fluid test problems, including a magma - ideal gas shocktube and a helium cylinder - shock wave interaction problem.

### *Keywords:*

cut-cell, space-time discontinuous Galerkin, front tracking, level set, two fluid flow.

---

## 1. Introduction

In part I [19] a space-time discontinuous Galerkin (STDG) finite element method for two fluid flows was presented. This space-time discontinuous Galerkin (STDG) finite element method offers high accuracy, an inherent ability to handle discontinuities and a very local stencil, making it relatively easy to combine with local *hp*-refinement. For the interface handling a front tracking approach is used because front tracking methods are capable of high accuracy. The front tracking is implemented using cut-cell mesh refinement

---

\*Corresponding author.

*Email addresses:* [w.e.h.sollie@math.utwente.nl](mailto:w.e.h.sollie@math.utwente.nl) (W.E.H. Sollie),  
[j.j.w.vandervegt@math.utwente.nl](mailto:j.j.w.vandervegt@math.utwente.nl) (J.J.W. van der Vegt )

because this type of refinement is very local in nature and hence combines well with the STGD. To compute the interface dynamics the level set method (LSM) is used, because of its ability to deal with merging and breakup, because it was expected that the LSM combines well with the cut-cell mesh refinement and also because the LSM is easy to extend to higher dimensions. The small cell problem caused by the cut-cell refinement was solved by using a merging procedure involving bounding box elements, which improves stability and performance of the method. The interface conditions can be incorporated in the numerical flux at the interface and the STDG discretization ensures that the scheme is conservative as long as the numerical fluxes are conservative.

In this article the method is applied to a number of model problems in two and three space-time dimensions which range from one dimensional linear advection tests to complex two fluid problems including a magma - ideal gas shock tube test and a shock wave - helium cylinder interaction test. The interface is assumed to be clean and without surface tension and therefore continuity of the normal velocity and pressure is imposed [8, 18]. The simulations have been performed using three dimensional space-time codes based on the *hp*GEM software framework for Discontinuous Galerkin finite element methods [14].

The outline of this article is as follows. First, in Section 2, the two fluid flow error measure is defined. In Section 3, the HWENO slope limiter is introduced. In Sections 4-8 the test results are presented. Finally, in Section 9, a discussion with conclusions is given.

## 2. Error measurement

Let  $w_h^i(t_{n+1}, \mathbf{x})$  denotes the approximate flow solution,  $w^i(t_{n+1}, \mathbf{x})$  the exact flow solution and  $\Omega_h^i(t_{n+1})$  the spatial mesh for fluid  $i$  at time  $t = t_{n+1}$ . The  $L_2$  flow error at time  $t = t_{n+1}$  is defined as:

$$\|w_h^i(t_{n+1}, \cdot) - w^i(t_{n+1}, \cdot)\|_{L_2(\Omega_h^i(t_{n+1}))} = \left( \int_{\Omega_h^i(t_{n+1})} |w_h^i(t_{n+1}, \mathbf{x}) - w^i(t_{n+1}, \mathbf{x})|^2 d\mathbf{x} \right)^{1/2}. \quad (1)$$

The order of accuracy with respect to the norm  $\|\cdot\|$  is defined as  $\log(\|f_h - f\|/\|f_{h/2} - f\|)/\log(2)$ , where  $f_h$  and  $f_{h/2}$  denote numerical solutions on embedded meshes  $\Omega_h^n$  and  $\Omega_{h/2}^n$ , with  $h$  the mesh width. It should be noted

that the refined meshes are often only approximately embedded, hence a small error is introduced in the orders of accuracy for the flow solutions.

The STDG method has order of accuracy  $O(h^{p+1})$  for smooth solutions and order of accuracy  $O(h^{1/2})$  for discontinuous solutions ([12, 20]). Front capturing and tracking techniques can help to improve the accuracy of the STDG method around discontinuities.

Solutions will be plotted as discontinuous data without any postprocessing to give a clear illustration of the behavior of the STDG numerical scheme in each individual element.

### 3. Slope limiter

Around strong discontinuities which are not captured or tracked DG solutions show spurious oscillations. To control these oscillations the Hermite WENO slope limiter introduced in [13] is used. The limiter is applied after every physical time step to the spatial solution at the most recent time level. Since a space-time mesh is used, this means the limiter is applied at time slab faces. Let  $\mathcal{S}_e^{n+1}$  denote a time slab face on which the solution requires limiting. The solution after slope limiting is defined as the weighted sum of a number of reconstructed polynomials  $P_i(u_h), i = 1, \dots, N_P$ :

$$\tilde{u}_h = \sum_{i=1}^{N_P} w_i P_i(u_h), \quad (2)$$

where  $u_h$  denotes the numerical solution on  $\mathcal{S}_e^{n+1}$ ,  $\tilde{u}_h$  the limited solution on  $\mathcal{S}_e^{n+1}$  and  $N_P$  the number of reconstructed polynomials. The weights are defined as:

$$w_i = \frac{(\epsilon + o_i(P_i))^{-\gamma}}{\sum_{k=0}^{N_P-1} (\epsilon + o_k(P_k))^{-\gamma}}, \quad (3)$$

with  $\epsilon > 0$  and  $\gamma > 0$  constants. Here  $o_i(P_i)$  denotes the oscillation indicator for element  $\mathcal{K}_e$ :

$$o_i(P_i) = \|\bar{\nabla} P_i\|_{L_2(\mathcal{S}_i^{n+1})}, \quad (4)$$

with  $\|\cdot\|_{L_2(\mathcal{S}_i^{n+1})}$  the  $L_2$  norm at time slab face  $\mathcal{S}_i^{n+1}$  and  $\bar{\nabla}$  the space gradient operator.

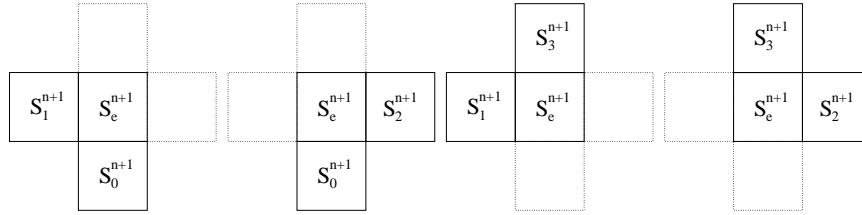


Figure 1: Lagrange stencils for quadrilateral shaped time slab faces.

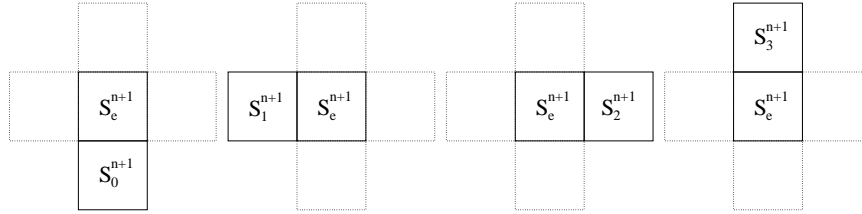


Figure 2: Hermite stencils for quadrilateral shaped time slab faces.

Each polynomial  $P_i(u_h)$  is constructed from the numerical solution  $u_h$  on a specific stencil  $S_i$  of time slab faces, where the shape of the stencil depends on the type of reconstruction polynomial and the shape of the face  $\mathcal{S}_e^{n+1}$ . Three types of reconstruction polynomials are considered: Lagrange, Hermite, and, the linear projection of the original polynomial. The corresponding stencils are shown for quadrilateral shaped faces in Figures 1, 2 and 3, respectively. For the Lagrange polynomials, the stencil is composed of the face  $\mathcal{S}_e^{n+1}$  and also  $d$  of the  $N_n$  neighboring faces  $\mathcal{S}_{l_{i,j}}^{n+1}$ ,  $j = 0, \dots, d-1$ , where  $d$  denotes the space dimension and  $l_{i,j} \in \{0, \dots, N_n\}$ . For the Hermite polynomials, every stencil is composed of just two time slab faces, namely the face  $\mathcal{S}_e^{n+1}$  and one neighboring face  $\mathcal{S}_h^{n+1}$  where  $h \in \{0, \dots, N_n\}$ . For the linear projection the stencil is composed only of the face  $\mathcal{S}_e^{n+1}$ .

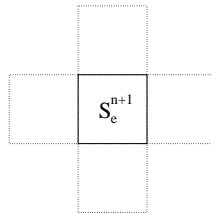


Figure 3: Stencil used for the restriction of the original polynomial for quadrilateral shaped time slab faces.

Each Lagrange polynomial  $P_{L,i}$  is constructed using only the solution averages for the time slab faces of the Lagrange stencil. Let  $x_e, x_a$  and  $x_b$  denote the face midpoints in physical coordinates for the time slab faces  $\mathcal{S}_e^{n+1}, \mathcal{S}_{l_i,0}^{n+1}$  and  $\mathcal{S}_{l_i,1}^{n+1}$ . The reconstructed Lagrange polynomial  $P_{L,i}$  is defined as:

$$\begin{aligned} \frac{1}{|\mathcal{S}_e^{n+1}|} \int_{\mathcal{S}_e^{n+1}} P_{L,i} dK &= \frac{1}{|\mathcal{S}_e|} \int_{\mathcal{S}_e^{n+1}} u_h dK \\ \frac{1}{|\mathcal{S}_{l_i,0}^{n+1}|} \int_{\mathcal{S}_{l_i,0}^{n+1}} P_{L,i} dK &= \frac{1}{|\mathcal{S}_{l_i,0}^{n+1}|} \int_{\mathcal{S}_{l_i,0}^{n+1}} u_h dK \\ \frac{1}{|\mathcal{S}_{l_i,1}^{n+1}|} \int_{\mathcal{S}_{l_i,1}^{n+1}} P_{L,i} dK &= \frac{1}{|\mathcal{S}_{l_i,1}^{n+1}|} \int_{\mathcal{S}_{l_i,1}^{n+1}} u_h dK \end{aligned} \quad (5)$$

with  $i = 0, \dots, 3$  and  $l_i \in \{(0, 1), (0, 2), (1, 3), (2, 3)\}$  for quadrilateral shaped time slab faces. Each Hermite reconstruction polynomial  $P_{H,i}$  is constructed from the solution average in the time slab face  $\mathcal{S}_e^{n+1}$  and the average solution gradient from one neighbour time slab face and is defined as:

$$\begin{aligned} \frac{1}{|\mathcal{S}_e^{n+1}|} \int_{\mathcal{S}_e^{n+1}} P_{H,i} dK &= \frac{1}{|\mathcal{S}_e^{n+1}|} \int_{\mathcal{S}_e^{n+1}} u_h dK \\ \frac{1}{|\mathcal{S}_e^{n+1}|} \int_{\mathcal{S}_e^{n+1}} \frac{\partial P_{H,i}}{\partial x} dK &= \frac{1}{|\mathcal{S}_{h_i}^{n+1}|} \int_{\mathcal{S}_{h_i}^{n+1}} \frac{\partial u_h}{\partial x} dK \\ \frac{1}{|\mathcal{S}_e^{n+1}|} \int_{\mathcal{S}_e^{n+1}} \frac{\partial P_{H,i}}{\partial y} dK &= \frac{1}{|\mathcal{S}_{h_i}^{n+1}|} \int_{\mathcal{S}_{h_i}^{n+1}} \frac{\partial u_h}{\partial y} dK \end{aligned} \quad (6)$$

with  $h_i = i$  and  $i = 0, \dots, 3$  for quadrilateral shaped time slab faces. The linear projection of the original polynomial  $P_O$  is treated as a Hermite reconstruction polynomial, with  $\mathcal{S}_b^{n+1} = \mathcal{S}_e^{n+1}$  and is defined as:

$$\begin{aligned} \frac{1}{|\mathcal{S}_e^{n+1}|} \int_{\mathcal{S}_e^{n+1}} P_O dK &= \frac{1}{|\mathcal{S}_e^{n+1}|} \int_{\mathcal{S}_e^{n+1}} u_h dK \\ \frac{1}{|\mathcal{S}_e^{n+1}|} \int_{\mathcal{S}_e^{n+1}} \frac{\partial P_O}{\partial x} dK &= \frac{1}{|\mathcal{S}_e^{n+1}|} \int_{\mathcal{S}_e^{n+1}} \frac{\partial u_h}{\partial x} dK \\ \frac{1}{|\mathcal{S}_e^{n+1}|} \int_{\mathcal{S}_e^{n+1}} \frac{\partial P_O}{\partial y} dK &= \frac{1}{|\mathcal{S}_e^{n+1}|} \int_{\mathcal{S}_e^{n+1}} \frac{\partial u_h}{\partial y} dK \end{aligned} \quad (7)$$

The slope limiter only needs to be active at places where the solution displays strong discontinuities and for this purpose the discontinuity detector proposed by Krivodonova [11] is used. The discontinuity factor  $\mathcal{I}$  of a numerical solution  $u_h$  at the time slab face  $\mathcal{S}^{n+1}$  is defined as:

$$\mathcal{I} = \frac{|\int_{\partial\mathcal{S}_e^{n+1}}(u_h^- - u_h^+)de|}{h^{(p+1)/2}|\partial\mathcal{S}^{n+1}|\|u_h^-\|_{L_\infty}}, \quad (8)$$

where  $u_h^-$  and  $u_h^+$  denote the solution traces from the inside and the outside of the time slab face, at time  $t_{n+1}$  and considering only space directions,  $\partial\mathcal{S}_e^{n+1}$  denotes the time slab face boundary, which is composed of a number of finite element edges, and  $h$  is the radius of the circle circumscribing  $\mathcal{S}_e^{n+1}$ . The solution is assumed to be smooth when  $\mathcal{I} < \mathcal{I}_0$  and discontinuous when  $\mathcal{I} > \mathcal{I}_0$ , with  $\mathcal{I}_0$  a constant parameter determining the amount of limiting.

#### 4. Linear advection

Considered first are a number of single fluid linear advection problems in one space dimension. The purpose of these tests is to check the accuracy of the STDG method without interface tracking, for continuous and discontinuous solutions, respectively, and also to investigate the effect of interface tracking on the accuracy for a discontinuous solution. In all test cases linear basis functions are used.

The linear advection equation:

$$\frac{\partial\rho}{\partial t} + a\frac{\partial\rho}{\partial x} = 0, \quad (9)$$

with  $\rho$  the advection variable and  $a = 5 \text{ m/s}$  the advection velocity, is solved on a spatial domain  $[-5 \text{ m}, 5 \text{ m}]$  from time  $t = 0 \text{ s}$  to  $1 \text{ s}$ . Continuous and discontinuous initial conditions are defined as:

$$\rho(t, x) = \rho_0(x) = \begin{cases} 1.5 + 0.5 \cos(\pi(x + 2.5)) & \text{for } |x + 2.5| \leq 1 \text{ m} \\ 1.0 & \text{for } |x + 2.5| > 1 \text{ m}, \end{cases} \quad (10)$$

and

$$\rho(t, x) = \rho_0(x) = \begin{cases} 2.0 & \text{for } x < -2.5 \text{ m} \\ 1.0 & \text{for } x > -2.5 \text{ m}, \end{cases} \quad (11)$$

Table 1: Error and order of accuracy in the  $L_2$  norm of the advection variable in the linear advection test with smooth initial conditions (10) and without interface tracking.

$N_x \times N_t$	$L_2$ error	$L_2$ order
$20 \times 10$	0.287488	–
$40 \times 20$	0.0986332	1.543
$80 \times 40$	0.0212308	2.216
$160 \times 80$	0.00459294	2.209

Table 2: Error and order of accuracy in the  $L_2$  norm of the advection variable for the linear advection test with discontinuous initial conditions (11) and without interface tracking.

$N_x \times N_t$	$L_2$ error	$L_2$ order
$20 \times 10$	0.327226	–
$40 \times 20$	0.255301	0.358
$80 \times 40$	0.198344	0.364
$160 \times 80$	0.1537	0.368

respectively. At the inflow boundary Dirichlet boundary conditions are used:

$$\rho(t, x) = \rho_0(x) \text{ at } x = -5 \text{ m} \quad (12)$$

Since this is a single fluid test, an upwind flux is used everywhere. The exact solution to (9) is:

$$\rho(x, t) = \rho_0(x - at). \quad (13)$$

The simulations are performed at  $CFL_{\Delta t} = 1.0$ .

First, the method is tested for the smooth initial solution (10) without mesh refinement. The solution at time  $t = 1 \text{ s}$  is illustrated in Figure 4 (left). The results are presented in Table 1, where the  $L_2$  errors and corresponding orders of accuracy are given for various mesh resolutions. Orders of accuracy of approximately 2 are observed, which is as expected since the STDG is of order  $O(h^{p+1})$  for smooth solutions.

Second the method is tested for the discontinuous initial solution (11) without mesh refinement. The solution at time  $t = 1 \text{ s}$  is illustrated in Figure 4 (right). Near the interface spurious oscillations are visible. The results are presented in Table 2, where the  $L_2$  errors and the corresponding orders of accuracy are given for various mesh resolutions. In the  $L_2$  norm the orders of accuracy are approximately 0.36, which is as expected since for discontinuous solutions computed on a static mesh the order of accuracy will typically not exceed  $O(h^{1/2})$ .

Third the method is tested for a discontinuous initial solution (11) with mesh refinement. The numerical solution at time  $T = 1 \text{ s}$  and the refined

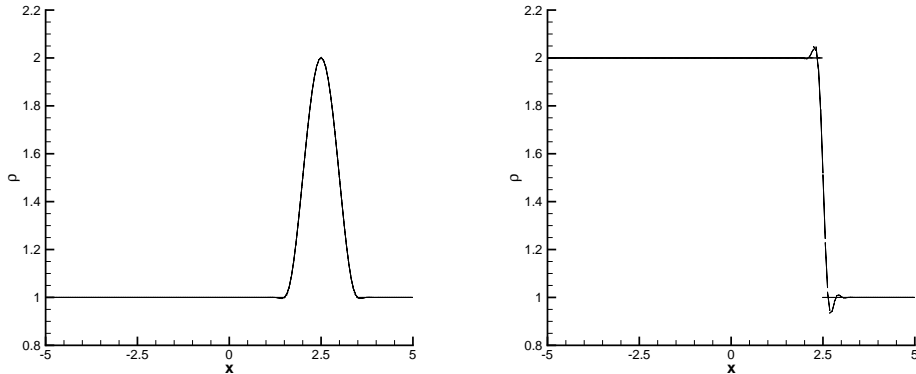


Figure 4: The exact (dotted) and numerical (solid) solutions at time  $t = 1$  s of the linear advection tests without mesh refinement for continuous (left) and discontinuous initial conditions (right) using 160 elements.

space-time mesh using 20 elements are shown in Figure 5. The performance of the two fluid scheme is optimal for this test, with the error in the solution and the interface position both at machine precision. This is the case because the interface movement is linear in space-time; hence, the interface is represented exactly in the refined mesh.

Fourth, the method is tested for a non constant advection velocity  $a = -x$  m/s, a discontinuous initial solution (11) and with mesh refinement. The exact solution is given as:

$$\rho(t, x) = \rho_0(xe^t). \quad (14)$$

and the exact interface position at time  $t$  is  $x_{IF}(t) = -2.5 e^{-t} m$ . In this test the discontinuity moves nonlinearly; hence, it cannot be represented exactly in the mesh. In Figure 6 the space-time mesh and solution are shown for a mesh of 20 elements and it is observed that the discontinuity is not resolved very well. The results are presented in Table 4.

Fifth, the same case as in the fourth test is considered, but at the discontinuity solid wall conditions are applied, implemented as a zero flux. By using solid wall conditions at the discontinuity, it is treated as an interface; hence, the problem is considered as a two fluid problem. In Figure 7 solution is shown for a mesh of 20 elements. The interface is captured much better. The results are presented in Table 4. In the  $L_2$  norm the error converges to



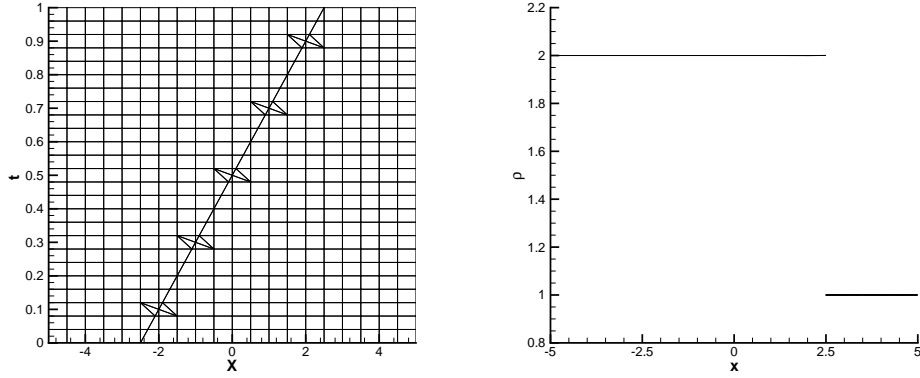


Figure 5: Space-time mesh and numerical solution at time  $t = 1$  s of the linear advection test with mesh refinement for discontinuous initial conditions using 20 elements.

Table 3: Error and order of accuracy in the  $L_2$  norm of the advection variable for the linear advection test with non constant velocity  $a = -x$  m/s and upwind flux at the discontinuity.

$N_x \times N_t$	$L_2$ error	$L_2$ order
$20 \times 10$	0.0408045	-
$40 \times 20$	0.0254312	0.682
$80 \times 40$	0.017552	0.535
$160 \times 80$	0.0117917	0.5739

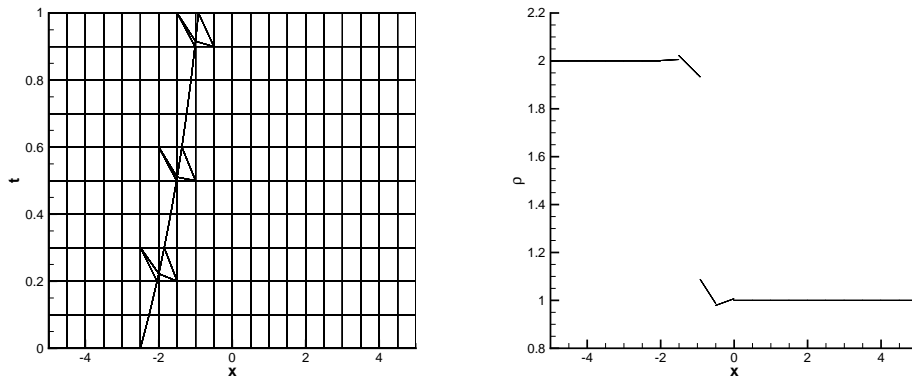


Figure 6: Space-time mesh and solution at time  $t = 1$  s for the linear advection test with non constant velocity  $a = -x$  using 20 elements and upwind flux at the discontinuity.

Table 4: Error and order of accuracy in the  $L_2$  norm of the advection variable for the linear advection test with non constant velocity  $a = -x m/s$  and solid wall flux at the discontinuity.

$N_x \times N_t$	$L_2$ error	$L_2$ order
$20 \times 10$	0.00112646	-
$40 \times 20$	0.000735784	0.614
$80 \times 40$	0.000736948	-0.00228
$160 \times 80$	0.000551662	0.4178

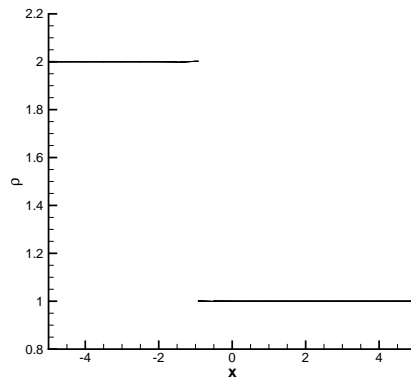


Figure 7: Solution at time  $t = 1 s$  for the linear advection test with non constant velocity  $a = -x m/s$  using 20 elements and solid wall flux at the discontinuity.

$O(h^{1/2})$ .

In conclusion, results were presented for a number of single fluid linear advection tests in one space dimension. For a uniform mesh and continuous and discontinuous solutions respectively the theoretical  $L_2$  orders of accuracy could be confirmed. The results for the discontinuous solution were improved greatly by applying mesh refinement to capture the discontinuity. In addition results were presented for a non constant advection velocity  $a = -x m/s$ . When using an upwind flux at the discontinuity, it was observed that the discontinuity could not be captured very well. When using a solid wall flux at the interface, the discontinuity could be captured much better.

## 5. Zalesak disc

In order to investigate how well the method can handle moving interfaces in two space dimensions, the Zalesak disc test problem [29] is examined. A disc, initially as shown in Figure 8, is rotated counterclockwise one period around the domain midpoint  $(x, y) = (0, 0) m$  with velocity  $\mathbf{u} = (-2\pi y, 2\pi x) m/s$ . The purpose of this test is to check the accuracy of the level set solution obtained with the discontinuous Galerkin method when the level set smoothing procedure is turned on. The test also serves to illustrate the two fluid mesh refinement. The most difficult part in this test consists of capturing the sharp corners of the disc. The level set equation is solved in two space dimensions on the domain  $[-4 m, 4 m] \times [-4 m, 4 m]$  from time  $t = 0 s$  to  $1 s$ .

The simulations are performed at  $CFL = 1.0$ . In Figure 9 the approximate disc at the initial and the final time is shown for  $80 \times 80$  and  $160 \times 160$  elements, respectively. The interface evolution for  $80 \times 80$  elements is shown in Figure 10. At the initial time the level set shows an error near the sharp edges of the disc, due to the fact that the nonlinear initial level set conditions cannot be represented exactly using piecewise linear polynomials. Also, after one rotation the level set solution shows a relatively large error near the sharp edges of the disc. It is expected that the results will improve by using a higher order level set approximation or by applying h-refinement. The latter option is preferred since in general the level set velocity will be obtained from the flow velocity and may not be of high order.

From the test results it is concluded that when sharp corners are present in the problem, the accuracy of the method is expected to suffer quite severely.

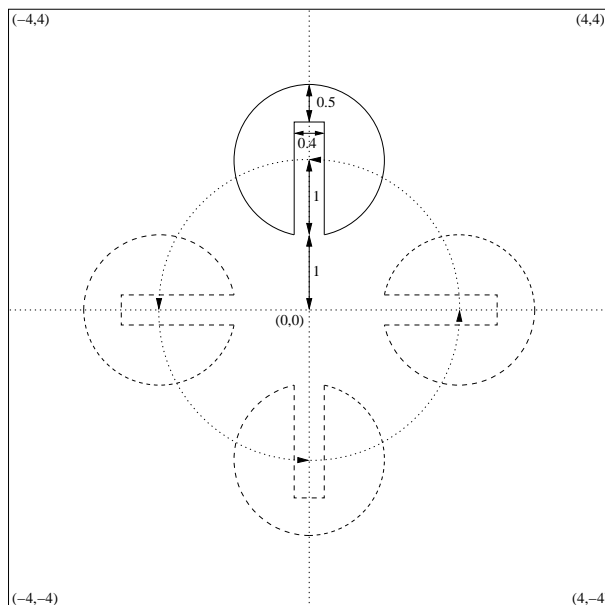


Figure 8: Zalesak disc test problem.

However, even for a smooth interface, small errors in the level set and interface position are likely to be present.

## 6. Sod's ideal gas shock tube

Considered is Sod's ideal gas shock tube test [23]. The purpose of this test is to investigate the performance of the method for a case where the interface moves with the flow velocity. To account for this, two solve steps are used for the flow and level set equations in each time step. The contact wave is considered an interface and is captured using the two fluid method.

The one dimensional Euler equations expressing conservation of mass, momentum and energy are defined as

$$\begin{aligned}
 \frac{\partial \rho}{\partial t} + \frac{\partial(\rho u)}{\partial x} &= 0 \\
 \frac{\partial(\rho u)}{\partial t} + \frac{\partial(\rho u^2 + p)}{\partial x} &= 0 \\
 \frac{\partial(\rho E)}{\partial t} + \frac{\partial(u(\rho E + p))}{\partial x} &= 0,
 \end{aligned} \tag{15}$$

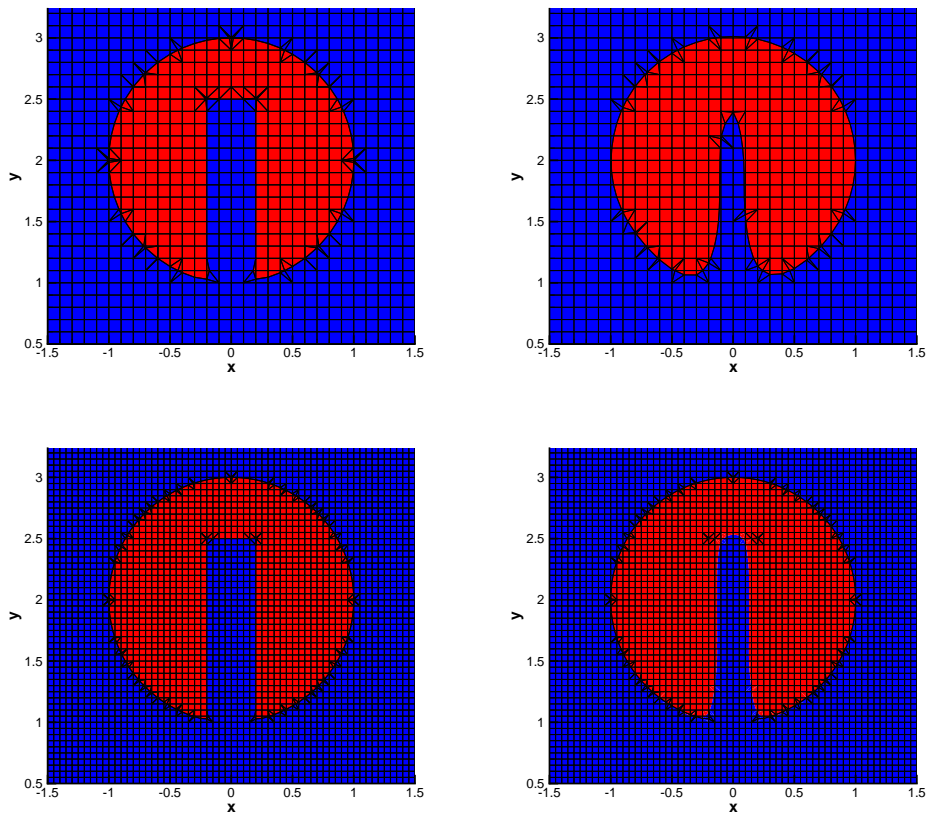


Figure 9: The refined mesh at the initial time (left) and after one rotation (right) for the Zalesak disc test problem for a mesh with  $80 \times 80$  (top)  $160 \times 160$  (bottom) elements.

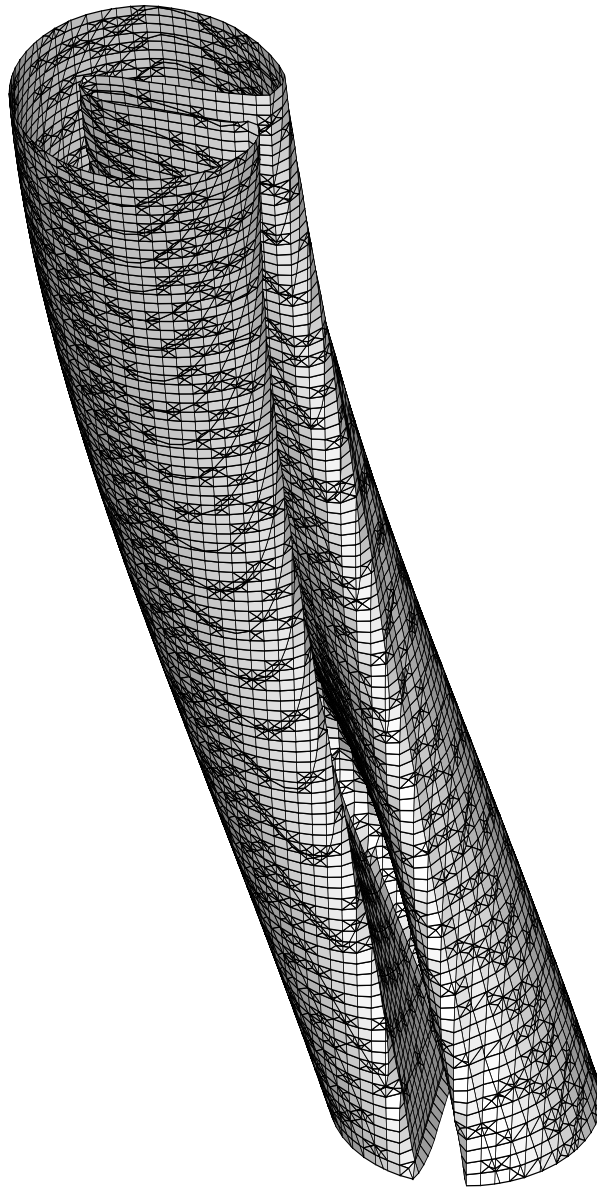


Figure 10: Interface evolution for the Zalesak disc test problem for the first 1/4 rotation for a mesh with  $80 \times 80$  elements.

with  $\rho$  the density,  $u$  the fluid velocity,  $p$  the pressure and  $\rho E = \rho u^2/2 + \rho e$  the total energy, with  $\rho e$  the internal energy. In addition to these equations an equation of state (EOS) is required to account for the thermodynamic properties of the ideal gas:

$$e = \frac{p}{\rho(\gamma - 1)}, \quad (16)$$

where  $\gamma = 1.4$ . The Euler equations are solved on a spatial domain  $[-5\text{ m}, 5\text{ m}]$  from time  $t = 0\text{ s}$  to  $0.01\text{ s}$ . Initially the interface is located at  $x = 0\text{ m}$  and both fluids are in constant states:

$$\begin{aligned} (\rho, u, p)(0, x) = & \quad (17) \\ \left\{ \begin{array}{ll} (\rho_L, u_L, p_L) = (2.37804\text{ kg/m}^3, 0\text{ m/s}, 2.0 \times 10^5\text{ Pa}) & \text{for } x < 0\text{ m} \\ (\rho_R, u_R, p_R) = (1.18902\text{ kg/m}^3, 0\text{ m/s}, 1.0 \times 10^5\text{ Pa}) & \text{for } x > 0\text{ m}. \end{array} \right. \end{aligned}$$

At the boundaries solid wall conditions are imposed:

$$u \cdot \bar{n} = 0 \text{ at } x = \pm 5\text{ m} \quad (18)$$

At the interface the velocity and pressure are continuous.

The solution to (15), illustrated in Figure 11, features an expansion wave moving to the left with head speed  $S_{LH} = -343.138\text{ m/s}$  and tail speed  $S_{LT} = -241.218\text{ m/s}$ , a contact wave moving to the right with speed  $S_C = 84.9331\text{ m/s}$  and a shock wave also moving to the right with speed  $S_R = 397.861\text{ m/s}$ . Between the expansion and the contact wave the solution is constant and equal to the left star state  $(\rho_L^*, u^*, p^*)$  and between the contact and the shock wave the solution is also constant and equal to the right star state  $(\rho_R^*, u^*, p^*)$ , where  $\rho_L^* = 1.84490\text{ kg/m}^3$ ,  $\rho_R^* = 1.51174\text{ kg/m}^3$ ,  $u^* = 84.9331\text{ m/s}$  and  $p^* = 1.40179 \times 10^5\text{ Pa}$ .

Let  $\mathbf{w} = (\rho, \rho u, \rho E)$  and  $\mathbf{F} = (\rho u, \rho u^2 + p, u(\rho E + p))$  denote the conservative variables and flux vectors. The HLLC flux provides an accurate solution to the Riemann problem, which is an initial value problem for the Euler equations, where the initial conditions consists of two constant states:

$$\mathbf{w}(x, 0) = \begin{cases} \mathbf{w}_L & \text{when } x < 0 \\ \mathbf{w}_R & \text{when } x > 0. \end{cases} \quad (19)$$

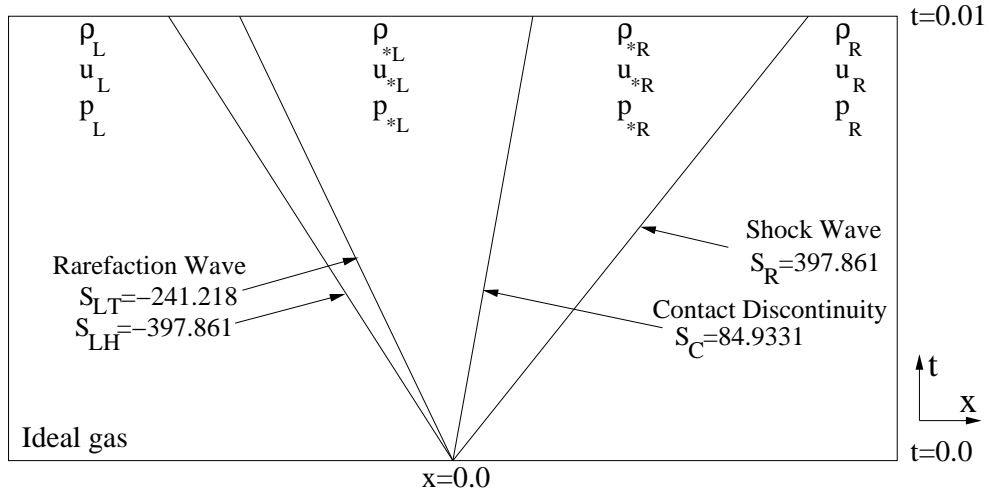


Figure 11: The solution structure of the ideal gas shock tube.

The HLLC flux extended to space-time meshes [3, 24] is defined as:

$$\begin{aligned} \mathcal{H}_{HLLC} = & \frac{1}{2} \left( \mathbf{F}_L + \mathbf{F}_R \right. \\ & - (|S_L - v| - |S_M - v|) \mathbf{w}_L^* + (|S_R - v| - |S_M - v|) \mathbf{w}_R^* \\ & \left. + |S_L - v| \mathbf{w}_L - |S_R - v| \mathbf{w}_R - v(\mathbf{w}_L + \mathbf{w}_R) \right), \end{aligned} \quad (20)$$

with  $v$  the interface velocity. It is assumed that the speeds are the same at both sides of the contact wave, so  $S_M = u_L^* = u_R^* = u^*$ . From the Rankine-Hugoniot relations  $\mathbf{F}(\mathbf{w}_K) - \mathbf{F}(\mathbf{w}_K^*) = S_K(\mathbf{w}_K - \mathbf{w}_K^*)$  with  $K = L$  or  $R$  for the left and the right waves, respectively, the following relations are found for the star state variables:

$$\begin{aligned} \rho_K^* &= \rho_K \frac{S_K - u_K}{S_K - u^*} \\ \rho_K^* u^* (u^* - S_K) &= (p_K - p^*) + \rho_K u_K (u_K - S_K), \end{aligned} \quad (21)$$

and also an approximation for the speed  $S_M = u^*$  of the contact wave is obtained:

$$S_M = \frac{\rho_R u_R (S_R - u_R) - \rho_L u_L (S_L - u_L) + p_L - p_R}{\rho_R (S_R - u_R) - \rho_L (S_L - u_L)}. \quad (22)$$



The wave speeds  $S_L$  and  $S_R$  are estimated as:

$$S_L = \min(u_L - a_L, u_R - a_R), \quad S_R = \max(u_L + a_L, u_R + a_R). \quad (23)$$

By using the Rankine-Hugoniot relations of the left wave and substituting the left and right states and wave speeds, the values of  $\mathbf{w}_L^*$  are calculated as:

$$\mathbf{w}_L^* = \frac{S_L - u_L}{S_L - S_M} \mathbf{w}_L + \frac{1}{S_L - S_M} \begin{pmatrix} 0 \\ p^* - p_L \\ p^* S_M - p_L u_L \end{pmatrix}, \quad (24)$$

and likewise for  $\mathbf{w}_R^*$  by replacing  $L$  with  $R$ . By using the expression for  $\rho_K^*$  and  $u^*$  in the Rankine-Hugoniot relation for the momentum of the left and the right moving wave, the intermediate pressure is found:

$$p^* = \rho_L(S_L - u_L)(S_M - u_L) + p_L = \rho_R(S_R - u_R)(S_M - u_R) + p_R. \quad (25)$$

The Euler equations are discretized using the set of primitive variables  $\mathbf{v} = (\rho, \mathbf{u}, p)$ . This is motivated by the observation that in many two fluid flow problems the velocity and often also the pressure are continuous across the interface while the momentum and energy are not. Since the conservative equations are used mass, momentum and energy are still conserved. The approximate primitive variables are defined as:

$$\mathbf{v}_h^{p,i}(t, \bar{\mathbf{x}})|_{\mathcal{K}_j^n} = \sum_m \hat{\mathbf{V}}_m^i(\mathcal{K}_j^{i,n}) \phi_m(t, \bar{\mathbf{x}}) \quad (26)$$

with  $\hat{\mathbf{V}}_m^i$  the primitive flow approximation coefficients. The discretized equations extended into pseudo-time become:

$$\tilde{M}_{mlkp}^{i,n} \frac{\partial \hat{V}_{pm}^{i,n}}{\partial \tau} + \mathcal{L}_{kl}^{i,n}(\hat{\mathbf{W}}^n(\mathbf{V}^n), \hat{\mathbf{W}}^{n-1}(\mathbf{V}^{n-1})) = 0 \quad (27)$$

with

$$\tilde{M}_{mlkp}^{i,n} = \int_{\mathcal{K}_j^{i,n}} \phi_l \phi_m \frac{\partial \mathbf{w}_k^i}{\partial \mathbf{v}_p^i} d\mathcal{K}. \quad (28)$$

The discretized equations are simplified by using evaluations in the element midpoints  $\mathbf{x}_{mid}$  and replacing the  $\psi_l \psi_m$  terms by the delta function  $\delta_{lm}$  in (28) to obtain:

$$\tilde{N}_{kp}^{i,n} \frac{\partial \hat{V}_{pl}^{i,n}}{\partial \tau} + \mathcal{L}_{kl}^{i,n}(\hat{\mathbf{W}}^n(\mathbf{V}^n), \hat{\mathbf{W}}^{n-1}(\mathbf{V}^{n-1})) = 0 \quad (29)$$

---

**Algorithm 1** Pseudo-time integration method for solving the non-linear algebraic equations in the space-time discretization.

---

1. Initialize first Runge-Kutta stage:  $\bar{\mathbf{V}}^{i,(0)} = \hat{\mathbf{V}}^{i,n}$ .
2. Calculate  $\bar{\mathbf{V}}^{i,(s)}$ ,  $s = 1, \dots, 5$ :

$$(1 + \alpha_s \lambda) \bar{\mathbf{V}}^{i,(s)} = \bar{\mathbf{V}}^{i,(0)} + \alpha_s \lambda \left( \bar{\mathbf{V}}^{i,(s-1)} - \Delta t (\tilde{N}^{i,n})^{-1} \mathcal{L}(\bar{\mathbf{W}}^{i,(s-1)}(\bar{\mathbf{V}}^{i,(s-1)}), \bar{\mathbf{W}}^{i,n-1}(\bar{\mathbf{V}}^{i,(n-1)})) \right)$$

3. Update solution:  $\hat{\mathbf{V}}^{i,n} = \bar{\mathbf{V}}^{i,(5)}$ .
- 

with

$$\tilde{N}_{kp}^{i,n} = |\mathcal{K}_j^{i,n}| \frac{\partial \mathbf{w}_k^i}{\partial \mathbf{v}_p^i}(\mathbf{x}_{mid}). \quad (30)$$

To account for the change in variables the Runge-Kutta pseudo time integration method is modified with  $\tilde{\mathbf{N}}$  in the following way:

At the interface the HLLC flux for a contact discontinuity is used. Assuming the interface coincides with the contact wave,  $S_M = v$  and the corresponding HLLC flux defines the contact HLLC flux  $\mathcal{H}_{HLLC}^C$ :

$$\mathcal{H}_{HLLC}^C = \frac{1}{2} \left( \mathbf{F}_L + \mathbf{F}_R + (S_M - S_L)(\mathbf{w}_L - \mathbf{w}_L^*) + (S_M - S_R)(\mathbf{w}_R - \mathbf{w}_R^*) - S_M(\mathbf{w}_L + \mathbf{w}_R) \right). \quad (31)$$

By inserting the expressions for  $\mathbf{w}_K^*$ , it follows that:

$$\mathcal{H}_{HLLC}^C = (0, p^*, p^* u^*)^T \quad (32)$$

which shows that there is no mass flux through the contact interface. At the domain boundary faces the solid wall conditions are implemented in the HLLC flux by defining the right state as:

$$\rho_R = \rho_L, u_R = -u_L, p_R = p_L. \quad (33)$$

The simulations are performed at  $CFL_{\Delta t} \approx 0.4$ .

The test results using the contact flux (32) are presented in Table 5. The solution converges in the  $L_2$  norm. In Figure 12 the evolution of the

Table 5: Error and order of accuracy in the  $L_2$  norm of the density for the ideal gas Euler shock tube test using the contact interface flux.

$N_x \times N_t$	$L_2$ error	$L_2$ order
$40 \times 40$	0.0708762	—
$80 \times 80$	0.0484641	0.548
$160 \times 160$	0.0296357	0.710
$320 \times 320$	0.0213965	0.467

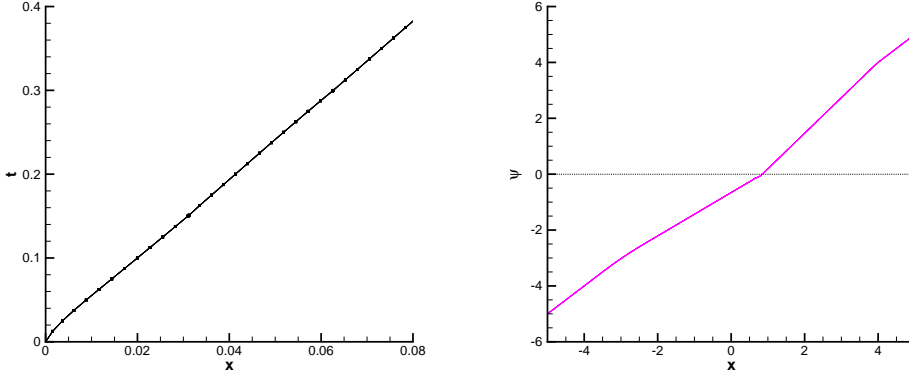


Figure 12: The time evolution of the interface and level set solution at time  $t = 0.01$  s for the ideal gas shock tube using 320 background elements, the contact flux and no slope limiter.

interface position for the first few time steps and the level set at the final time are shown. It is observed that in the first few time steps the interface moves too slow. The density, density zoom, velocity and pressure profiles at the final time are shown in Figure 13. Because the interface moves too slow initially, small undershoots are created in the density at the interface, which remain in the numerical solution until the final time. Small oscillations are also observed in the density, velocity and pressure profiles which radiate outwards from the interface.

In order to diminish the observed oscillations at the interface, an alternative interface flux is proposed, which is defined separately for the left and right sides of the interface:

$$\begin{aligned}
 \mathcal{H}_{HLLC}^L &= \mathbf{w}_L^*(S_M - v) + \mathcal{H}_{HLLC}^C \\
 \mathcal{H}_{HLLC}^R &= \mathbf{w}_R^*(S_M - v) + \mathcal{H}_{HLLC}^C
 \end{aligned} \tag{34}$$

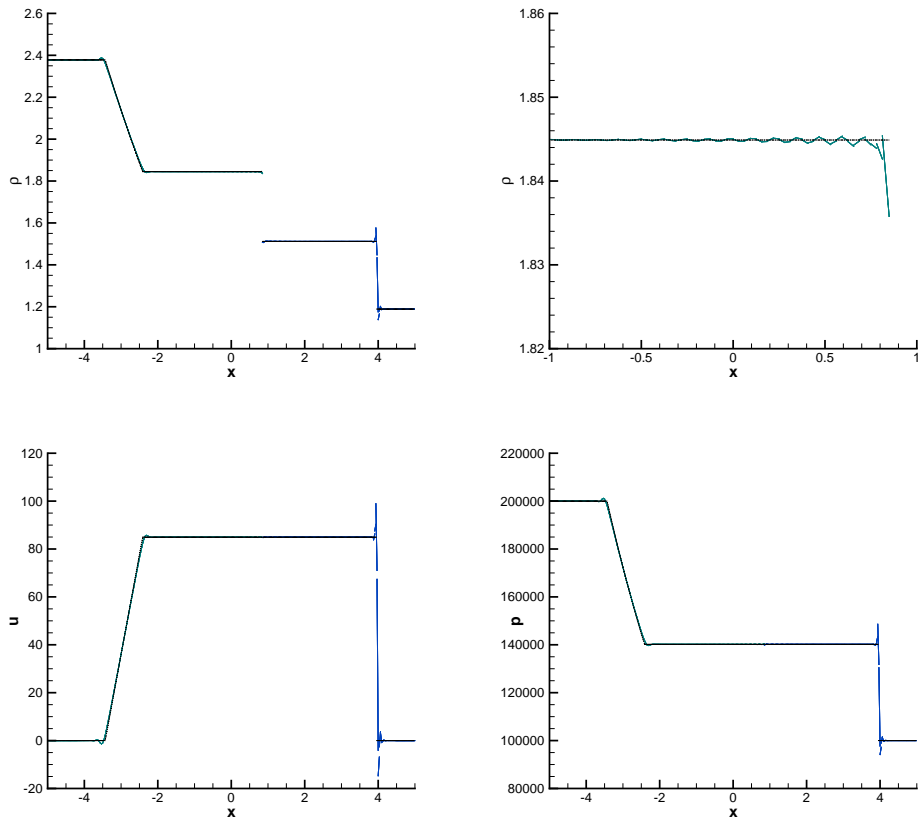


Figure 13: The exact (dotted) and numerical (solid) density, density zoom, velocity and pressure at time  $t = 0.01$  s for the ideal gas shock tube using 320 background elements, the contact flux and no slope limiter.

Table 6: Error and order of accuracy in the  $L_2$  norm of the density for the ideal gas Euler shock tube test with interface tracking and using the interface flux (34).

$N_x \times N_t$	$L_2$ error	$L_2$ order
$40 \times 40$	0.0729742	—
$80 \times 80$	0.0492437	0.567
$160 \times 160$	0.0300191	0.714
$320 \times 320$	0.0217169	0.467

When the interface representation in the mesh is exact,  $S_M = v$  and the interface flux is reduced to  $\mathcal{H}_{HLLC}^C$ . The interface numerical flux now removes the small numerical oscillations caused by errors in the interface shape and position at the cost of mass conservation at the interface. The results with the interface flux (34) are presented in Table 6. The solution converges in the  $L_2$  norm. In Figure 14 the density, density zoom, velocity and pressure profiles at the final time with the interface flux (34) are shown. Again, the interface moves too slow initially, causing undershoots in the density at the interface, which remains in the numerical solution until the final time. The density, velocity and pressure profiles do not show the oscillations observed before with the contact interface flux. In Figure 15 the mass evolution of the two fluids is shown. The mass loss is very small for this test.

In order to remove the spikes appearing near the expansion and shock waves in the solution with the interface flux (34) the HWENO slope limiter is used, and in Figure 16 the resulting density, density zoom, velocity and pressure profiles at the final time are shown. The slope limiter reduces the spikes at the expansion and shock waves. However, a small offset error is observed in the density, velocity and pressure profiles in the star region.

Finally, the simulation is run without the initial time steps, from  $t = T/10$  to  $t = T$ . The resulting density profile is shown in Figure 17. The results are much better than those obtained previously, especially near the interface. This is because the error made in the first number of time steps, when the rarefaction, contact and shock waves are too close to each other to be resolved well numerically, remains in the simulation for all subsequent time.

In conclusion, the two fluid method has been applied to Sod's shock tube test. Using a contact interface flux oscillations were observed at the interface. An alternative interface flux (34) was developed, reducing the oscillations at the interface at the cost of conservation. The interface flux (34) was tested with promising results. Using the slope limiter reduced the spikes near the expansion and shock waves, but introduced a small offset error in the star

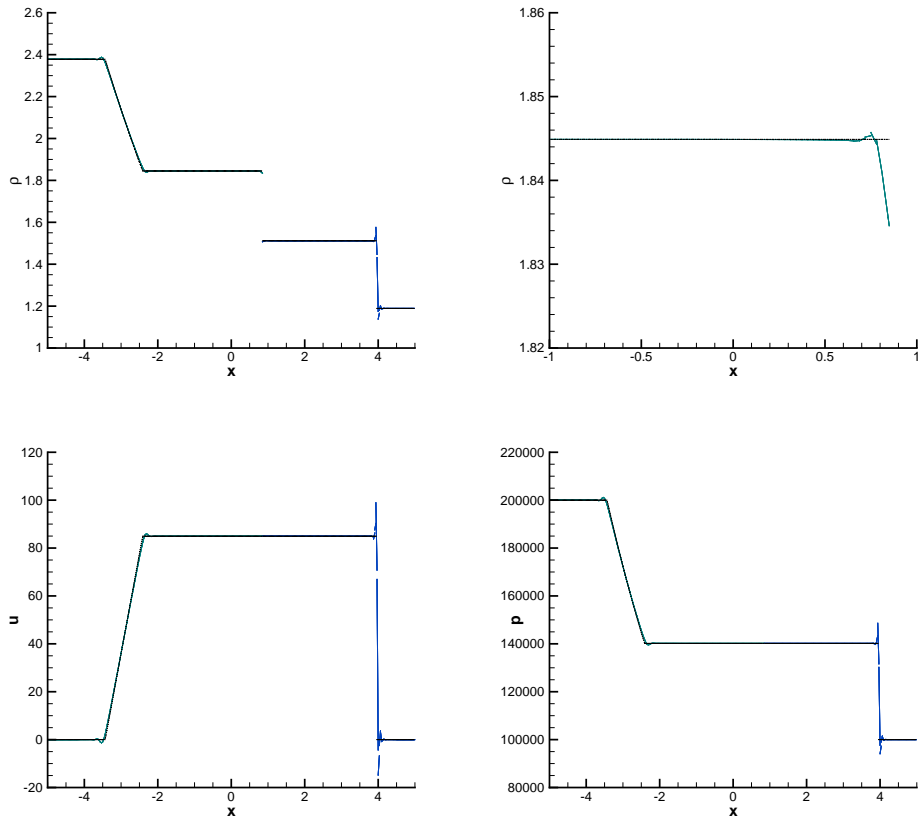


Figure 14: The exact (dotted) and numerical (solid) density, density zoom, velocity and pressure at time  $t = 0.01$  s for the ideal gas shock tube using 320 background elements, interface flux (34) and no slope limiter.

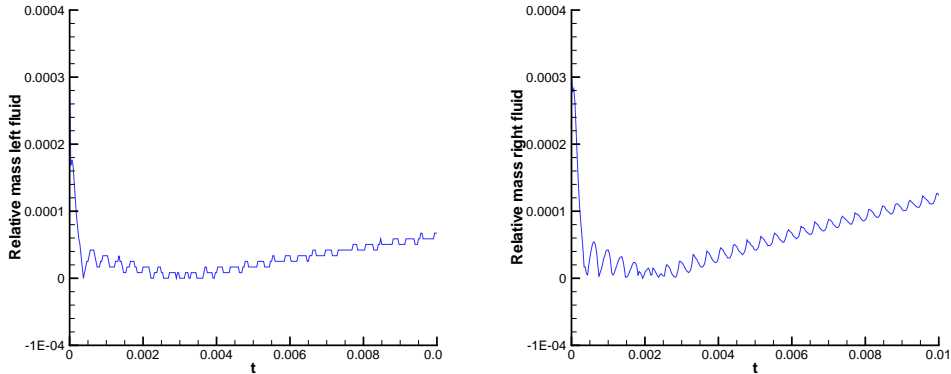


Figure 15: Relative mass over time of the left (left) and right (right) fluids for the ideal gas shock tube using 320 background elements, interface flux (34) and no slope limiter. The relative mass is defined as  $|M_e - M_h|/M_e$ , with  $M_e$  the exact and  $M_h$  the numerical amount of mass.

region. Starting the simulation at  $t = T/10$  greatly improved the numerical results.

## 7. Isothermal magma - ideal gas shock tube

Considered is an isothermal magma - ideal gas shock tube problem. This test is motivated by the high speed geological event analyzed in [4, 5, 6, 27] and [28] and it features very high density and pressure ratio's which cause strong oscillations around the interface between the gas and magma with standard shock capturing schemes. The governing equations for an effectively compressible magma are the Euler equations for mass and momentum:

$$\partial_t \mathbf{w} + \partial_x \mathbf{F}(\mathbf{w}) = 0, \quad (35)$$

with

$$\mathbf{w} = \begin{pmatrix} \rho \\ \rho u \end{pmatrix}, \quad \mathbf{F} = \begin{pmatrix} \rho u \\ \rho u^2 + p \end{pmatrix}. \quad (36)$$

For the ideal gas the one dimensional Euler equations (15) are used. The magma consists of a mixture of molten rock and 2 wt% (weight percentage)  $H_2O$ . At high pressure, the  $H_2O$  only has a liquid form. When the pressure

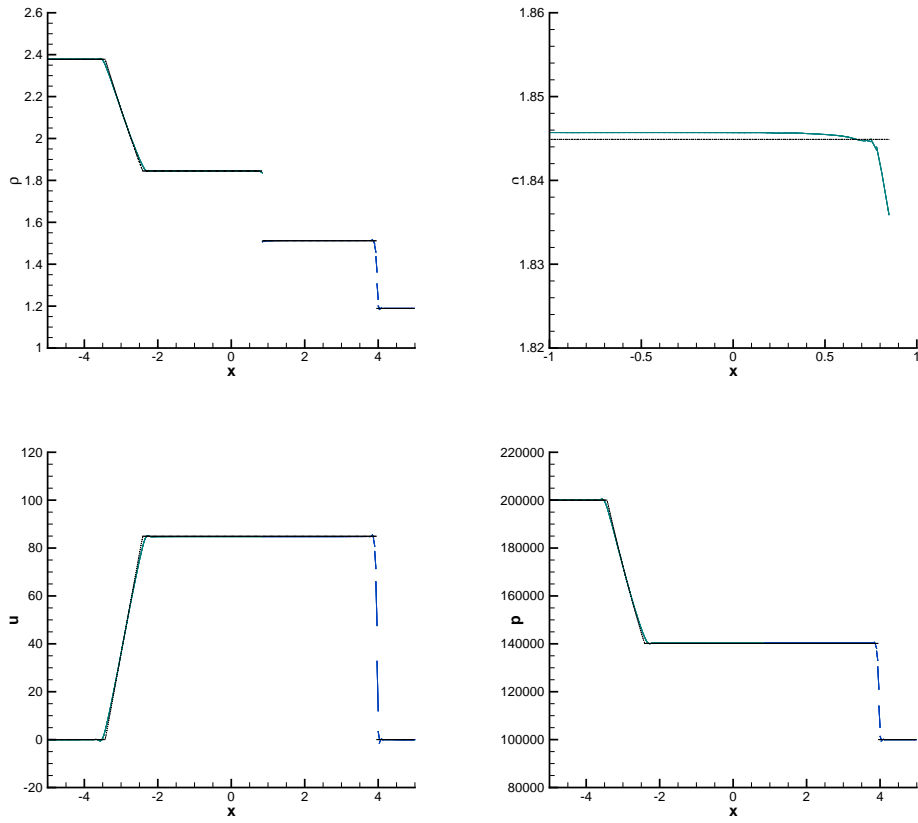


Figure 16: The exact (dotted) and numerical (solid) density, density zoom, velocity and pressure at time  $t = 0.01$  s for the ideal gas shock tube using 320 background elements, interface flux (34) and slope limiter.



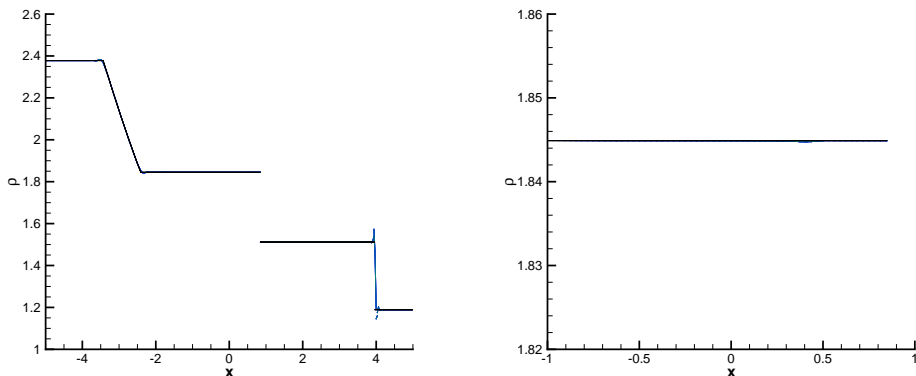


Figure 17: The exact (dotted) and numerical (solid) density and density zoom at time  $t = 0.01$  s for the ideal gas shock tube using 320 background elements, interface flux (34), no slope limiter and starting at initial time  $t = T/10$ .

decreases water vapor is formed within the mixture due to decompression effects. In this situation the magma effectively is a pseudo one-phase mixture. In explosive eruptions starting with a high pressure difference viscosity effects are negligible at leading order relative to the nonlinear inertial effects driven by the high bubble content. The total mass fraction  $n_0$  of  $H_2O$  in the magma consists of a fraction  $n(p)$  which is exsolved in the magma as gas and a fraction  $1 - n(p)$  which is dissolved in the magma as liquid.

The mixture of magma and liquid  $H_2O$  has a density  $\sigma = 2500 \text{ kg/m}^3$  and the water vapor has a density of  $\rho_g$ . The total void or bubble fraction of the mixture is given by  $\alpha = n(p)\rho/\rho_g$ . The density of the magma is defined as  $\rho = \alpha\rho_g + (1 - \alpha)\sigma$ . Using the relation for  $\alpha$  and the ideal gas law  $\rho_g = p/(RT)$  gives:

$$\rho = \left( \frac{n(p)R_m T}{p} + \frac{1 - n(p)}{\sigma} \right)^{-1}, \quad (37)$$

where  $R_m = 462 \text{ J/kgK}$  is the mixtures gas constant. This relation is only valid when there are bubbles, i.e.,  $n(p) > 0$ . The critical pressure  $p_c$  is reached when there are no longer any bubbles in the mixture. This is the case when  $n(p = p_c) = 0$  which gives  $p_c = (4/9) \times 10^8 \text{ Pa}$ . The magma considered will be assumed to be compressible; hence,  $p < p_c$ . For  $p \geq p_c$  the

following relation is used:

$$\rho = \sigma + c_m^{-2}(p - p_c), \quad (38)$$

with  $c_m = 2000 \text{ m/s}$  the speed of sound in bubble free magma. The mass fraction  $n(p)$  is assumed to satisfy Henry's law, which is valid when bubbles and melt are in equilibrium:

$$n(p) = n_0 - S_h p^\beta. \quad (39)$$

For basaltic high volatile magma,  $n_0 = 0.02$ ,  $\beta \approx 0.5$ ,  $T = 1200 \text{ K}$  and  $S_h = 3.0 \times 10^{-6} \text{ Pa}^{-\beta}$ . The magma is assumed to be isothermal at a temperature of  $1200 \text{ K}$ . For isothermal magma the density depends only on the pressure,  $\rho = \rho(p)$ . The speed of sound  $a$  is defined for isothermal magma as:

$$\begin{aligned} 1/a^2 &\equiv \left( \frac{\partial \rho}{\partial p} \right)_T = -\rho^2 \frac{\partial(1/\rho)}{\partial p} \\ &= -\rho^2 \left[ \frac{dn(p)}{dp} \left( \frac{R_m T}{p} + \frac{1}{\sigma} \right) - \frac{n(p) R_m T}{p^2} \right]. \end{aligned} \quad (40)$$

The simulations are performed on a spatial domain  $[-5 \text{ m}, 5 \text{ m}]$  from time  $t = 0 \text{ s}$  to  $t = 0.0075 \text{ s}$ . Initially the interface is located at  $x = 0 \text{ m}$ , with the magma on the left and the ideal gas on the right, and both fluids are in constant states:

$$\begin{aligned} (\rho, u, p)(0, x) &= \quad (41) \\ \left\{ \begin{array}{ll} (\rho_L, u_L, p_L) = (535.195 \text{ kg/m}^3, 0 \text{ m/s}, 5 \times 10^6 \text{ Pa}) & \text{for } x < 0 \text{ m} \\ (\rho_R, u_R, p_R) = (1.18902 \text{ kg/m}^3, 0 \text{ m/s}, 1.0 \times 10^5 \text{ Pa}) & \text{for } x > 0 \text{ m}. \end{array} \right. \end{aligned}$$

At the boundaries solid wall conditions are imposed:

$$u \cdot \bar{n} = 0 \text{ m/s at } x = \pm 5 \text{ m}. \quad (42)$$

At the interface continuity of the velocity and pressure is imposed. The exact solution is calculated by solving the magma and ideal gas Riemann problem and consists of a left moving expansion wave with head and tail speeds of  $S_{LH} = -97.2861 \text{ m/s}$ ,  $S_{LT} = 186.409 \text{ m/s}$  respectively, a contact wave which is identified with the magma-air interface and moves with speed  $S_C = 286.329 \text{ m/s}$ ; and, a right moving shock wave with speed  $S_R = 555.540 \text{ m/s}$ .

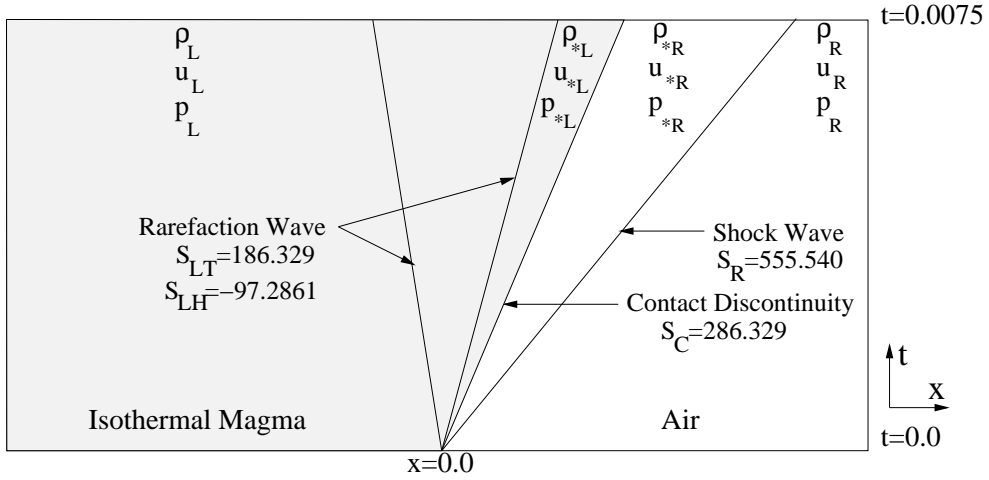


Figure 18: The solution structure of the Euler magma - ideal gas shock tube.

The left and right star states are defined as:  $\rho_L^* = 28.0517 \text{ kg/m}^3$ ,  $\rho_R^* = 2.45364 \text{ kg/m}^3$ ,  $u^* = 286.329 \text{ m/s}$ ,  $p^* = 2.89134 \times 10^5 \text{ Pa}$ . The solution structure is shown in Figure 18. At the interface the interface flux (34) is used, adapted for use with isothermal magma. With the contact interface flux (32) the simulations were not stable enough. At the boundary faces the solid wall conditions are implemented in the HLLC flux by defining the right state as:

$$\rho_R = \rho_L, u_R = -u_L, p_R = p_L. \quad (43)$$

To account for the dependence of the level set on the flow velocity the flow and level set are updated twice each time step. The simulations are performed at  $CFL_{\Delta t} \approx 0.56$ . Primitive variable discretizations are used for both fluids.

The test results for the solution at time  $t = 0.0075 \text{ s}$  using the interface flux (34) are presented in Table 7 and convergence in the  $L_2$  norm is observed. In Figure 19 the interface evolution over time and the level set profile at the final time are shown. Compared to the ideal gas shock tube test results, it takes much longer for the interface to reach the star velocity. Also, the level set becomes more distorted over time. The reason for this behavior lies in the use of the global flow velocity for advecting the level set. This problem can be fixed by reinitializing the level set every few time steps. In Figure 20 the density, density zoom, velocity and pressure at the final time using the interface flux (34) are shown. In Figure 21 the mass evolution for the magma and the ideal gas when using the interface flux (34) and without

Table 7: Error and order of accuracy in the  $L_2$  norm of the density for the isothermal magma and ideal gas Euler shock tube test using the interface flux (34).

$N_x \times N_t$	$L_2$ error	$L_2$ order
$40 \times 30$	28.5747	—
$80 \times 60$	16.7343	0.772
$160 \times 120$	10.6157	0.657
$320 \times 240$	5.95713	0.834

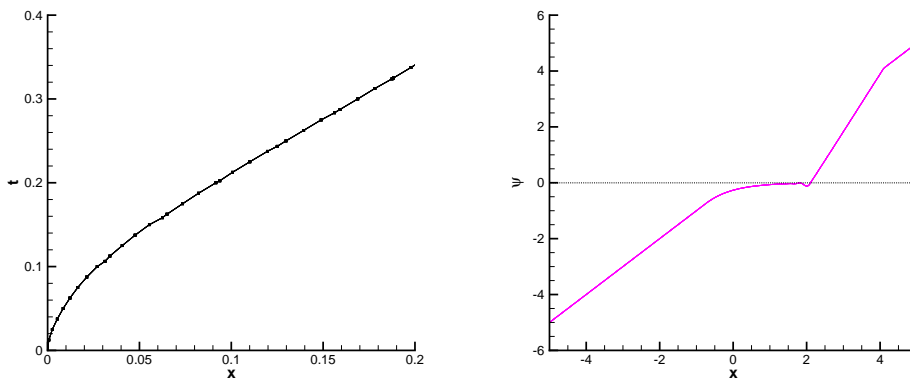


Figure 19: The time evolution of the interface position and level set at time  $t = 0.0075 s$  for the Euler magma - ideal gas shock tube using 320 background elements, interface flux (34) and no slope limiter.

slope limiter is shown. The amount of mass loss is negligible. In Figure 22 the density, density zoom, velocity and pressure at the final time using the interface flux (34) and the slope limiter are shown. Like in the shock tube test with the ideal gas, the slope limiter reduces the spikes at the shock wave but introduces a small offset error in the density, velocity and pressure profiles in the star region. Also, in the solution with the slope limiter the error in the shock position is visibly larger, probably because of the numerical dissipation added by the slope limiter to the flow velocity near the shock.

Finally, the simulation is run without the initial time steps, from  $t = T/10$  to  $t = T$ . The resulting density profile is shown in Figure 23. Because the error made in the first number of time steps remains is excluded in this simulation, the results are much better.

In conclusion, the two fluid method was used to solve a magma - ideal gas shock tube problem with the interface flux (34) with promising results. Using

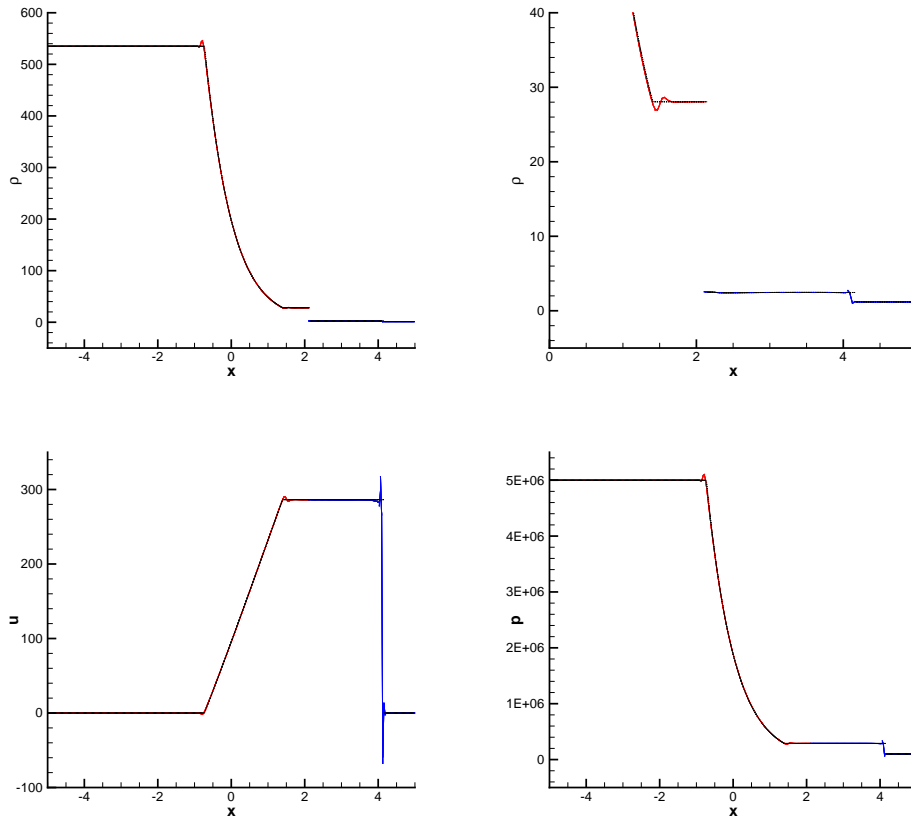


Figure 20: The exact (dotted) and numerical (solid) density, density zoom, velocity and pressure at time  $t = 0.0075$  s for the Euler magma - ideal gas shock tube using 320 background elements, interface flux (34) and no slope limiter.

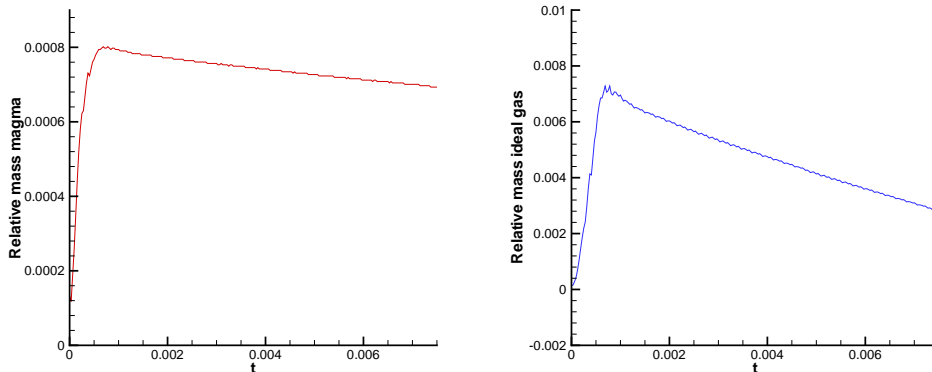


Figure 21: Relative mass over time of magma (left) and ideal gas (right) for the Euler magma - ideal gas shock tube using 320 background elements, interface flux (34) and no slope limiter. The relative mass is defined as  $|M_e - M_h|/M_e$ , with  $M_e$  the exact and  $M_h$  the numerical amount of mass.

the slope limiter reduced the spikes near the expansion and shock waves, but introduced a small offset error in the star region and also decreased the accuracy of the shock position. Starting the simulation at  $t = T/10$  greatly improved the numerical results. In this test the level set became very distorted, probably because of the advection with the global velocity. Periodic reinitialization of the level set can be used to solve this problem.

## 8. Helium cylinder - ideal gas shock interaction

To test the algorithm in a more complex setting computations are performed on the interaction between a cylindrical helium volume in a tube filled with an ideal gas and a Mach 1.22 shock wave [9, 10, 15, 26] as illustrated in Figure 24. For the Euler equations this problem has no unique solution, because the shock induces a Rayleigh-Taylor instability at the interface, but it presents a challenging test case for the numerical algorithm. The adiabatic indices and the gas constants for an ideal gas and helium are given as  $\gamma_I = 1.4$ ,  $R_I = 287.0 \text{ J/kgK}$  and  $\gamma_H = 1.67$ ,  $R_H = 2080.0 \text{ J/kgK}$ . Initially the helium volume is a cylinder with a radius  $0.025 \text{ m}$  and is located at  $(x, y) = (0 \text{ m}, 0 \text{ m})$  while the shock is located at  $x = 0.055625 \text{ m}$ . The domain has dimensions  $[-0.11125 \text{ m}, 0.11125 \text{ m}] \times [-0.0445 \text{ m}, 0.0445 \text{ m}]$ . Both fluids

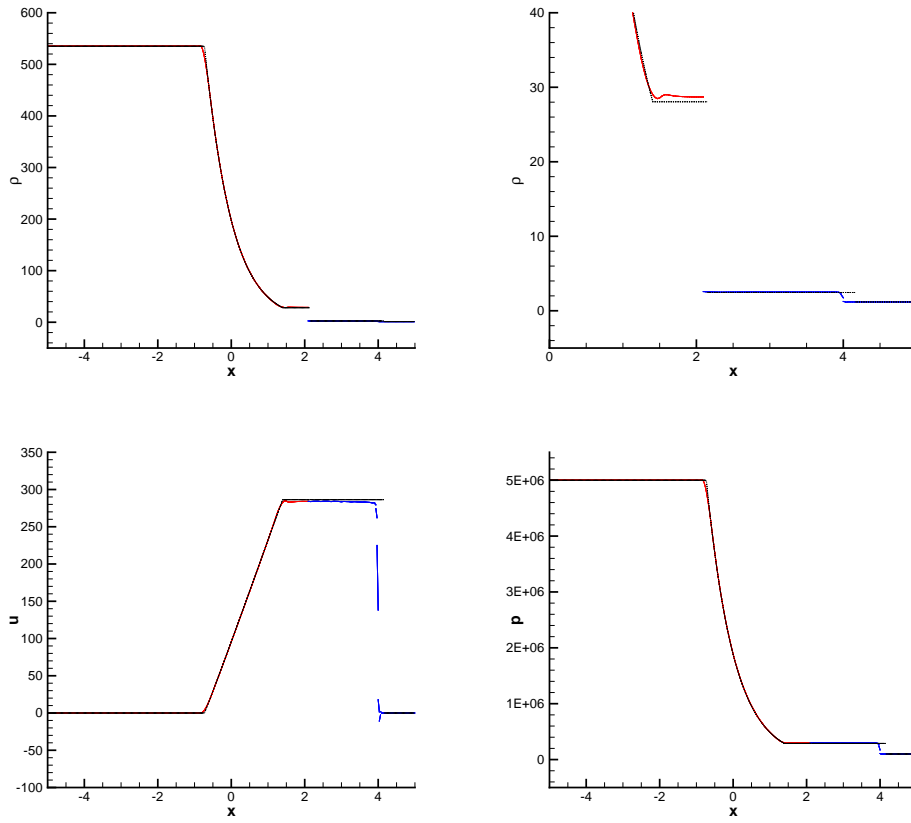


Figure 22: The exact (dotted) and numerical (solid) density, density zoom, velocity and pressure at time  $t = 0.0075$  s for the Euler magma - ideal gas shock tube using 320 background elements and the interface flux (34) and slope limiter.

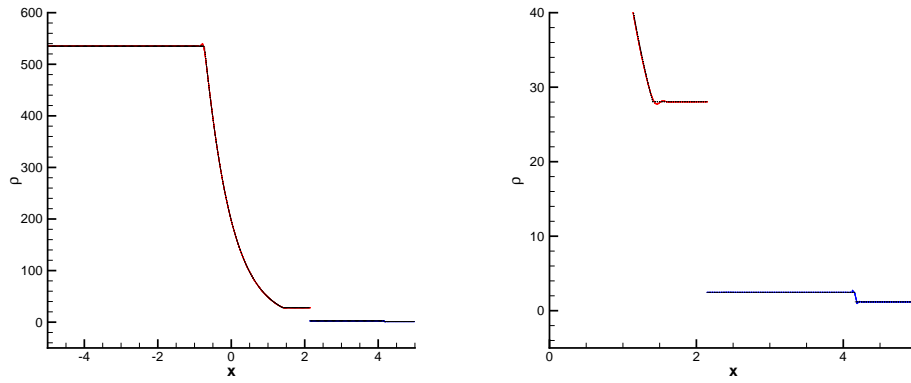


Figure 23: The exact (dotted) and numerical (solid) density and density zoom at time  $t = 0.0075$  s for the Euler magma - ideal gas shock tube using 320 background elements and the interface flux (34), no slope limiter and starting at initial time  $t = T/10$ .

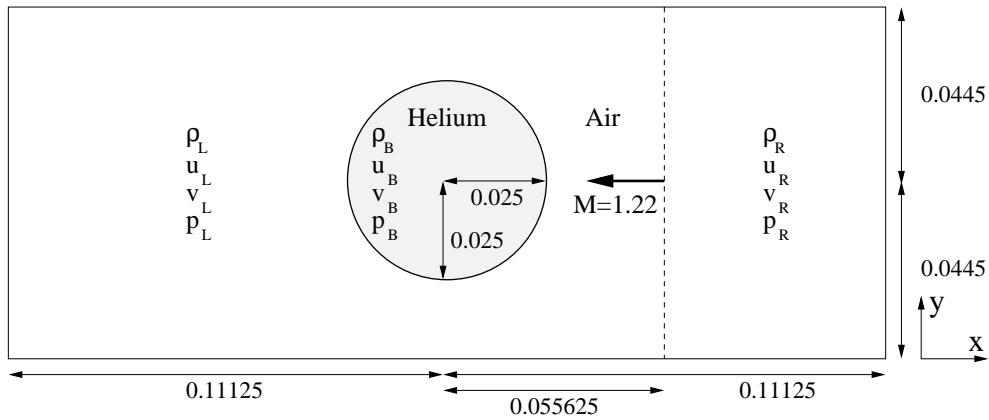


Figure 24: Helium cylinder - shock interaction test



are modelled using the two dimensional Euler equations. The initial state of the helium, and the ideal gas in front and behind of the shock are given as:

$$\begin{aligned}
(\rho_B, u_B, v_B, p_B) &= (0.164062 \text{ kg/m}^3, 0 \text{ m/s}, 0 \text{ m/s}, 1.0 \times 10^5 \text{ Pa}) \\
(\rho_L, u_L, v_L, p_L) &= (1.18902 \text{ kg/m}^3, 0 \text{ m/s}, 0 \text{ m/s}, 1.0 \times 10^5 \text{ Pa}) \\
(\rho_R, u_R, v_R, p_R) &= (1.63652 \text{ kg/m}^3, -114.473 \text{ m/s}, 0 \text{ m/s}, 1.5698 \times 10^5 \text{ Pa}),
\end{aligned} \tag{44}$$

where the density of the helium is related to the density of the air in front of the shock as  $\rho_B = \rho_L R_I / R_H$ . The shock velocity is  $V_S = Ma_L = 418.628 \text{ m/s}$ , with  $a_L = \sqrt{\gamma_I p_L / \rho_L} = 343.138 \text{ m/s}$ . The states on both sides of the shock wave are related through the Rankine-Hugoniot relations:

$$\begin{aligned}
(\rho_R - \rho_L)V_S &= (\rho_R u_R - \rho_L u_L) \\
(\rho_R u_R - \rho_L u_L)V_S &= (\rho_R u_R^2 - \rho_L u_L^2) + (p_R - p_L) \\
(\rho_R E_R - \rho_L E_L)V_S &= u_R(\rho_R E_R + p_R) - u_L(\rho_L E_L + p_L).
\end{aligned} \tag{45}$$

Using the definition of the total energy,  $\rho E = \rho(u^2 + v^2)/2 + \rho e$ , and the EOS for an ideal gas,  $\rho e = p/(\gamma_I - 1)$ , the Rankine-Hugoniot conditions can be solved for  $\rho_R, u_R$  and  $p_R$ .

When the initial shock wave incidents the upstream boundary of the helium volume, the shock is transmitted into the helium volume and accelerates due to the decrease in density, while the upstream boundary of the helium volume is set into downstream motion and an expansion wave is generated moving in the upstream direction. When the transmitted shock incidents the downstream boundary of the helium volume, the shock is transmitted and decelerates, while the downstream boundary of the helium volume is set into downstream motion and another expansion wave is generated moving in the upstream direction. Over time the helium volume flattens and is subsequently transformed into a vortex like structure. Basically the cylindrical helium volume acts as a divergent lens for the shock wave. In addition, the top wall adds to the complexity of the solution through a number of wave reflections.

At the top, bottom and left boundaries solid wall boundary conditions are imposed. At the right boundary the ideal gas state behind the shock is imposed weakly by using it as the external state of the numerical flux. At the interface continuity of the normal velocity and the pressure is imposed and the numerical flux (34) is used. To account for the dependence of the level set on the flow velocity the flow and level set are updated twice during

each time step. Because the solution is symmetric with respect to the x-axis, computations are performed on the half domain  $[-0.11125 m, 0.11125 m] \times [0 m, 0.0445 m]$ . The simulations are run using  $40 \times 8$ ,  $80 \times 16$ ,  $160 \times 32$  and  $320 \times 64$  elements from time  $t = 0 s$  to  $3.125 \times 10^{-4} s$  at  $CFL \approx 1.0$  using linear basis functions for the flow field and the level set, where the level set smoothing reconstructs a bilinear level set. By solving for a linear level set the Rayleigh-Taylor instability is effectively suppressed. Because the shock is not very strong the slope limiter is not used.

The density contours for subsequent times are shown in Figures 25 and 26. The mesh at time  $t = 3.4375 \times 10^{-4} s$  for different mesh resolutions is shown in Figures 27 and 28. The evolution of helium mass over time for different mesh resolutions is shown in Figure 29 and is relatively small. The mesh evolution is illustrated for  $80 \times 16$  elements in Figure 30.

In conclusion, the interaction between a helium cylinder and a shock wave was simulated using the interface flux (34). The mass loss was observed to be small.

## 9. Discussion

The space-time discontinuous Galerkin method with interface tracking has been applied to a number of one and two dimensional single and two fluid test problems.

1. Using a one dimensional linear advection test it was observed that the flow solution has approximate orders of accuracy of 2 for smooth initial conditions and 0.36 for discontinuous initial conditions, which matched theoretical orders of accuracy obtained in various studies. For the discontinuous solution, results improved when interface tracking was applied, because the interface could be captured exactly by mesh refinement. For a non-constant advection velocity it was observed that the interface tracking works quite well in combination with solid wall interface conditions.
2. The level set accuracy was tested using Zalesak's test. The level set solution was smoothed after each physical time step. It was observed that the influence of the limiting and smoothing was small. The shape of the disc after one rotation was preserved well at smooth area's of the disc, while in the neighborhood of the sharp corners the accuracy clearly suffered.

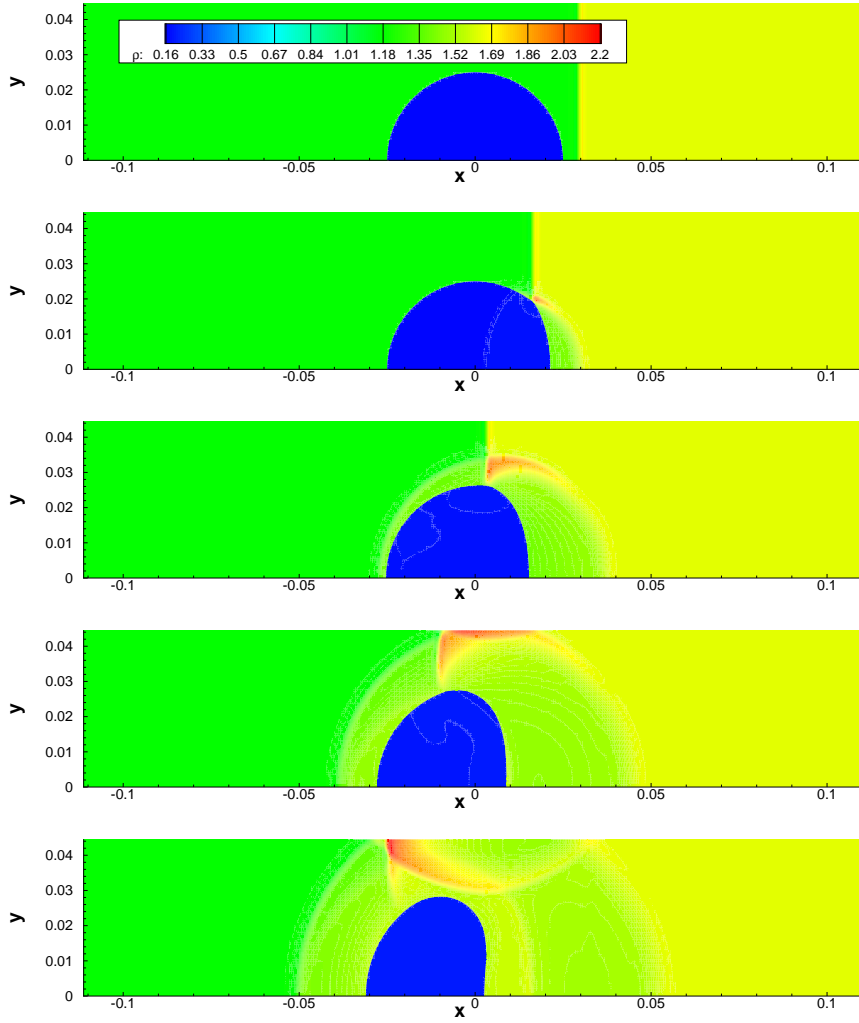


Figure 25: Density contours at times  $t = 0.625 \times 10^{-4} s, 0.9375 \times 10^{-4} s, 1.25 \times 10^{-4} s, 1.5625 \times 10^{-4} s, 1.875 \times 10^{-4} s$  for the helium cylinder - ideal gas shock interaction test using  $320 \times 64$  elements.

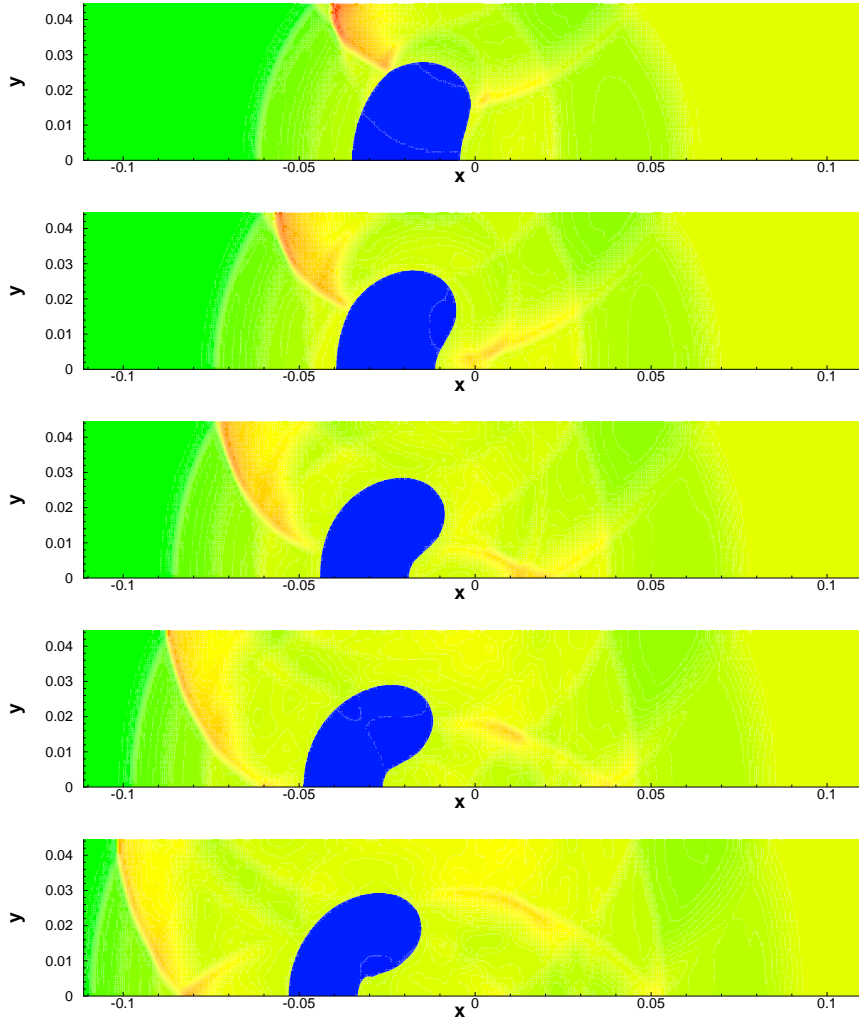


Figure 26: Density contours at times  $t = 2.1875 \times 10^{-4} s, 2.5 \times 10^{-4} s, 2.8125 \times 10^{-4} s, 3.125 \times 10^{-4} s, 3.4375 \times 10^{-4} s$  for the helium cylinder - ideal gas shock interaction test using  $320 \times 64$  elements.

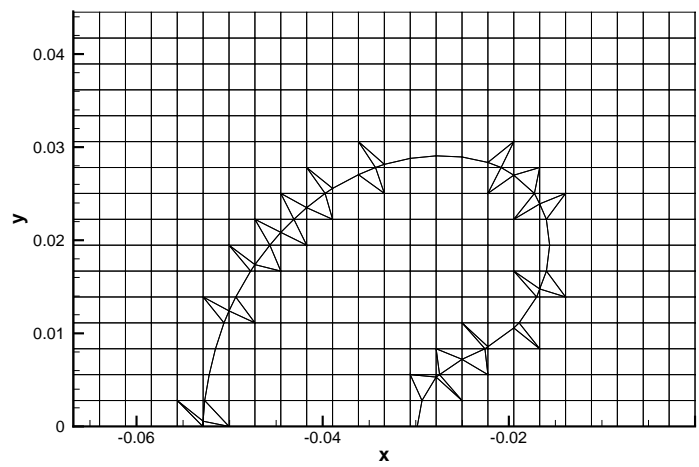
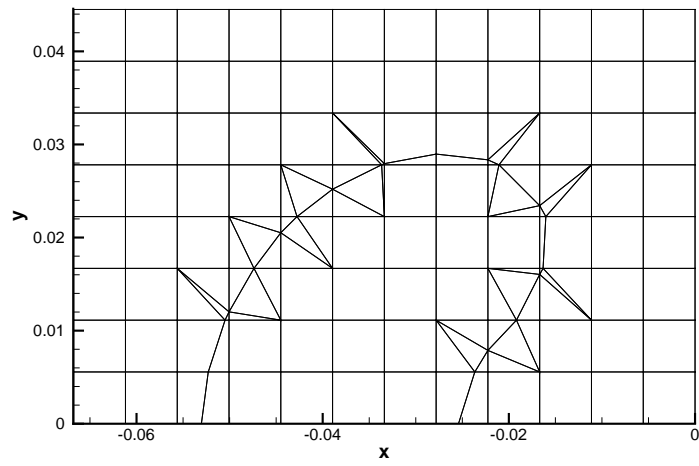


Figure 27: Mesh at time  $3.4375 \times 10^{-4} s$  for the helium cylinder - ideal gas shock interaction test using  $40 \times 8$  and  $80 \times 16$  elements.

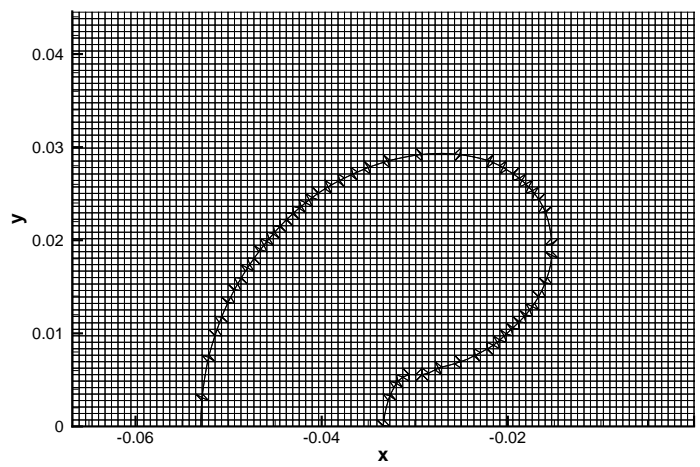
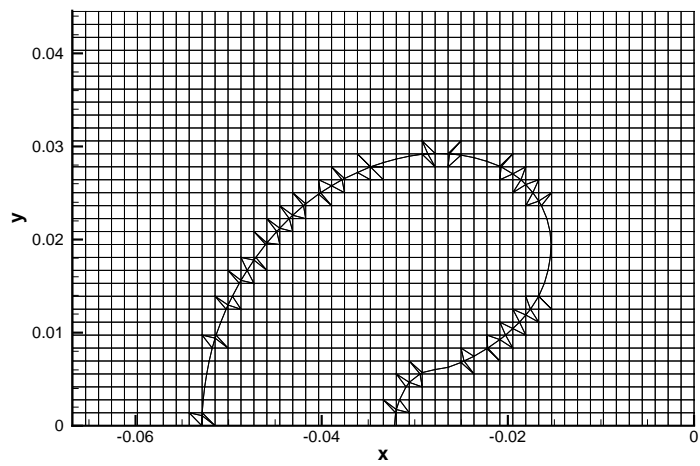


Figure 28: Mesh at time  $3.4375 \times 10^{-4} s$  for the helium cylinder - ideal gas shock interaction test using  $160 \times 32$  and  $320 \times 64$  elements.

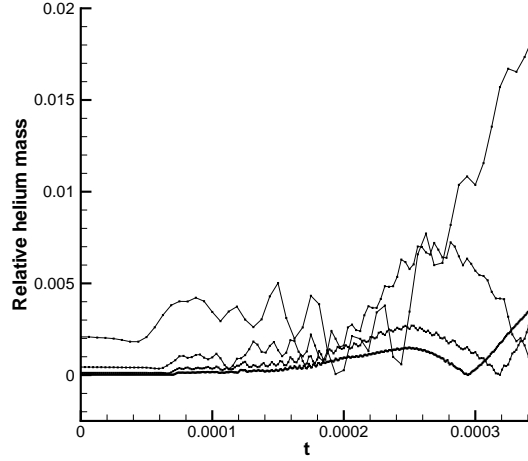


Figure 29: Relative helium mass over time for the helium cylinder - ideal gas shock interaction test using  $40 \times 8$ ,  $80 \times 16$ ,  $160 \times 32$  and  $320 \times 64$  elements. The relative mass is defined as  $|M_e - M_h|/M_e$ , with  $M_e$  the exact and  $M_h$  the numerical amount of mass.

3. The method was applied to a one dimensional ideal gas single fluid Euler shock tube problem. Using a contact interface flux, oscillations were observed at the interface. An alternative interface flux (34) was developed, which reduces the oscillations at the interface at the cost of a very small mass conservation error. The interface flux (34) was tested with promising results. Slope limiting reduced the spikes in the solution but also caused a decrease in accuracy. Starting the simulation at  $t = T/10$  greatly improved the results.
4. The method was applied to a magma - ideal gas shock tube. This test case featured two very different fluids and very high density and pressure ratio's. The method gave good results with the interface flux (34). Slope limiting reduced the spikes in the solution but also caused a decrease in accuracy. Starting the simulation at  $t = T/10$  greatly improved the results.
5. The method was applied to calculate the interaction between a helium cylinder and a shock wave using the interface flux (34). The mass loss was observed to be small.

Some interesting future applications involve:

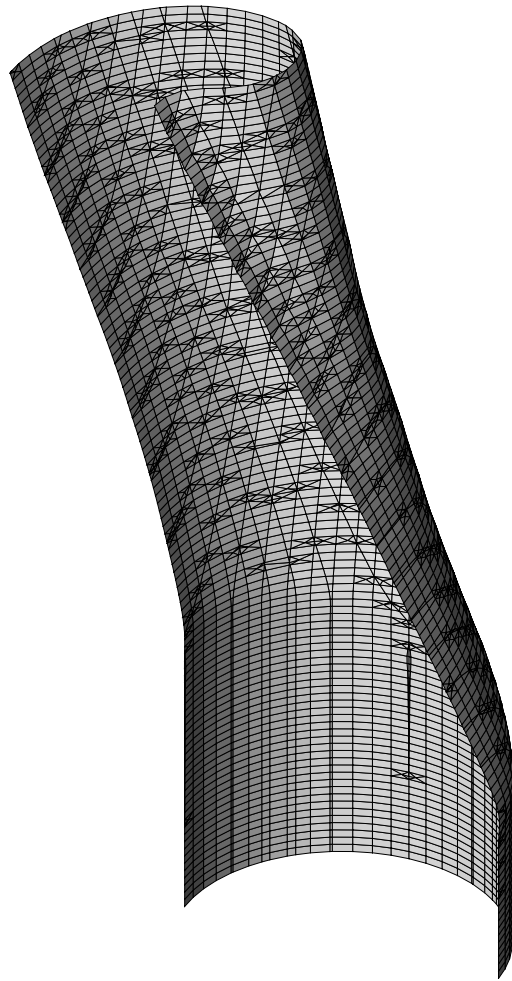


Figure 30: Interface evolution for the helium cylinder - ideal gas shock interaction test using  $80 \times 16$  elements.



- The shallow water equations to simulate flooding and drying [2, 3, 7, 16, 21] two-phase flows [17] and other applications [1, 22, 25]. Because of the methods' flexibility in defining flow domains with interfaces it is expected that valuable contributions are possible in these fields.
- The well known Rayleigh–Taylor and Kelvin-Helmholtz instability tests, which are interesting because they feature extreme interface deformation.
- Interface related phenomena with the method including interface curvature, tension and contamination, chemical reactions and membranes, which play a role in many real life two-fluid problems.

### Acknowledgments

The author is kindly indebted to V.R.Ambati, A.Bell, O.Bokhove and L.Pesch for the valuable discussions, suggestions and support.

### References

- [1] B. Akers, O. Bokhove, Hydraulic Flow through a Channel Contraction: Multiple Steady States, *Phys.Fluids*, 20 (2008) 056601.
- [2] V.R. Ambati, Flooding & drying in discontinuous Galerkin discretizations of shallow water equations, ECCOMAS Egmond aan zee, European Conference on Computational Fluid Dynamics, (2006), <http://proceedings.fyper.com/eccomasfd2006/>.
- [3] V.R. Ambati, O. Bokhove, Space-time discontinuous Galerkin discretization of rotating shallow water equations, *J. Comp. Phys.*, 225 (2007) 1233–1261.
- [4] O. Bokhove, Numerical modeling of magma-repository interactions, University of Twente, 97 pp, (2001), <http://eprints.eemcs.utwente.nl/>.
- [5] O. Bokhove, Decompressie van magma in opslagtunnels. *Nederlands Tijdschrift voor Natuurkunde* 68 (2002) 232–235, English version: <http://eprints.eemcs.utwente.nl/>.
- [6] O. Bokhove, A.W. Woods, A. de Boer, Magma Flow through Elastic-Walled Dikes, *Theor. Comp. Fluid Dyn.* 19 (2005) 261–286.

- [7] O. Bokhove Flooding & drying in finite-element Galerkin discretizations of shallow-water equations. Part I: One dimension, *J. Sci. Comp.* 22 (2005) 47-82.
- [8] D.A. Edwards, H. Brenner, D.T. Wasan, *Interfacial processes & rheology.* Butterworth-Heineman, Stoneham, Reed publishing, 1991.
- [9] R.P. Fedkiw et al., A Non-Oscillatory Eulerian Approach to Interface in Multimaterial Flows (The Ghost Fluid Method), *J. Comp. Phys.* 152 (1999) 457–492.
- [10] J.-F. Haas, B. Sturtevant, Interaction of weak shock waves with cylindrical & spherical gas inhomogeneities, *J. Fluid Mech.* 181 (1987) 41–76.
- [11] L. Krivodonova et al., Shock detection & limiting with discontinuous Galerkin methods for hyperbolic conservation laws. *Appl. Num. Math.* 48 (2004) 323–338.
- [12] Kröner, *Numerical schemes for conservation laws*, Wiley und Teubner, 1996.
- [13] H. Luo, J.D. Baum, R. Lohner, A Hermite WENO-based limiter for discontinuous Galerkin method on unstructured grids, *J. Comp. Phys.* 225 (2007) 686–713.
- [14] L. Pesch et al., hpGEM- A software framework for discontinuous Galerkin finite element methods, *ACM Transactions on Mathematical Software*, 33 (2007).
- [15] J. Qiu, T. Liu, B.C. Khoo, Simulations of Compressible Two-Medium Flow by Runge-Kutta Discontinuous Galerkin Methods with the Ghost Fluid Method, *Commun. Comp. Phys.* 3-2 (2008) 479–504.
- [16] J.-F. Remacle et al., An adaptive discretization of shallow-water equations based on discontinuous Galerkin methods, *Int. J. Numer. Meth. Fluids* 52 (2006) 902–923.
- [17] S. Rhebergen, O. Bokhove, J.J.W. van der Vegt, Discontinuous Galerkin finite element method for shallow two-phase flows, *Comp. Methods Appl. Mech. Engrg.* 198 (2009) 819-830.

- [18] L.E. Scriven, Dynamics of a fluid interface, *Chem. Eng. Sci.* 12 (1960) 98–108.
- [19] W.E.H. Sollie, O. Bokhove, J.J.W. van der Vegt, Two Fluid Space-Time Discontinuous Galerkin Finite Element Method, Part I: Theory, (2009), <http://eprints.eemcs.utwente.nl/>.
- [20] J.J. Sudirham, J.J.W. van der Vegt, R.M.J. van Damme, Space-time discontinuous Galerkin method for advection-diffusion problems on time-dependent domains, *Appl. Num. Math.* 56 (2006) 1491–1518
- [21] P.A. Tassi, O. Bokhove, C.A. Vionnet, Space discontinuous Galerkin method for shallow water flows-kinetic & HLLC flux, & potential vorticity generation, *Advances in Water Resources* 30 (2007).
- [22] P.A. Tassi et al., A discontinuous Galerkin finite element model for bed evolution under shallow flows, *Comp. Methods Appl. Mech. Eng.* 197 (2008) 2930-2947.
- [23] E. F. Toro, *Riemann solvers & numerical methods for fluid dynamics*, Springer Verlag, Berlin, 1997.
- [24] J.J.W. van der Vegt, H. van der Ven, Space-time discontinuous Galerkin finite element method with dynamic mesh motion for Inviscid Compressible Flows, *J. Comp. Phys.* 182 (2002) 546–585.
- [25] S.W. Vreman et al., Supercritical shallow granular flow through a contraction: experiment, theory & simulation, *J. Fluid Mech.* 578 (2007) 233-269.
- [26] J. Wackers, B. Koren, A fully conservative model for compressible two-fluid flow, *Int. J. Numer. Meth. Fluids* 47 (2005) 1337–1343.
- [27] A.W. Woods et al., Modeling magma-drift interaction at the proposed high-level radioactive waste repository at Yucca Mountain, Nevada, USA, *Geophys. Res. Lett.* 29 (2002) 1641.
- [28] A.W. Woods et al., Compressible magma flow in a two-dimensional elastic-walled dike, *Earth Planet. Sci. Lett.* 246 (2006) 241-250.
- [29] S.T. Zalesak, Fully multidimensional flux-corrected transport algorithms for fluids, *J. Comp. Phys.* 31 (1979) 335-362.